8th International Workshop on Microsystems

Alexander Campus, International Hellenic University, 20 December 2023

Workshop Proceedings

Introduction

This workshop brings together research and development from a large spectrum of science and engineering fields related to the implementation of microsystems in the new era of distributed information technologies. As cloud computing services and smart portable systems are becoming ubiquitous and more advanced, new possibilities for interdisciplinary research emerge. The microsystems that comprise the so-called internet of things will encompass a wide range of technologies including new energy sources, energy and information electronics, sensor systems, smart and energy efficient control and computing, telecommunications and networking, and also nanotechnology and micro-electro-mechanical systems. Continuing seven successful workshops between 2016 and 2022, the 8th International Workshop on Microsystems aims at bringing together related research and development advancements from the academic community and the industry. Scientific topics include but are not limited to:

Energy microsystems	Industrial automation and control
Sensors and sensor electronics	Microelectronics and nanoelectronics
Embedded systems	Micro-electro-mechanical systems
Integrated Circuits and Systems	Computing for microsystems

Michail E. Kiziroglou
m.kiziroglou@ihu.gr

Venue

Lecture Theater, [Automation and Informatics Building](#)

Alexander Campus, International Hellenic University, Greece
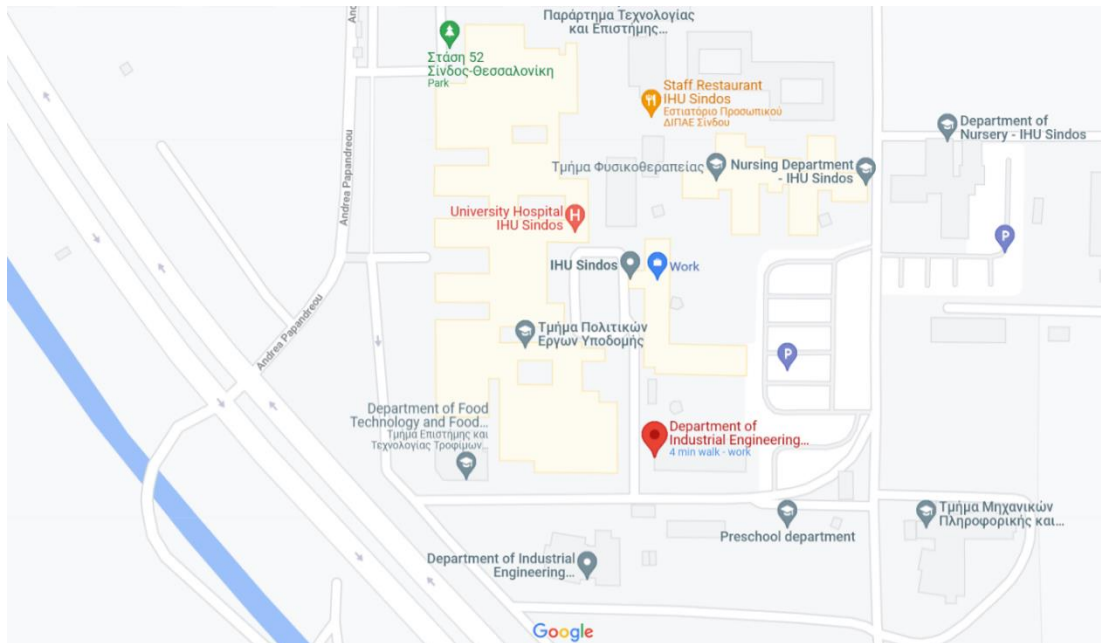
Date

Wednesday, 20th of December, 2023

Organizer

Michail E. Kiziroglou

Session Chairs

Dr. Eirini Aivazidou, Industrial Engineering & Management, IHU, Greece

Dr. Argyris Hatzopoulos, Information and Electronic Systems Engineering, IHU, Greece

Dr. Theodoros Kosmanis, Industrial Engineering & Management, IHU, Greece

Dr. Dimitrios Tziourtzioumis, Industrial Engineering & Management, IHU, Greece

Dr. Vagia Papanikolaou, Industrial Engineering & Management, IHU, Greece

Technical Programme Committee

Alexandros Astaras	Kostas Siozios
Dimitrios Bechtsis	Fotis Stergiopoulos Dimitrios
Alkiviadis Hatzopoulos	Tziourtzioumis
Michail E. Kiziroglou	Apostolos Tsagaris
Theodoros Kosmanis	Dimitris Triantafyllidis
Simira Papadopoulou	Christos Yfoulis

Organization and Technical Support

Alexandra Chatzimpaloglou, Ippokratis Kochliaridis

List of Authors

No	Last Name	First Name	Affiliation
1	Anagnostaki	Triantafyllia	IEM, International Hellenic University, Greece
2	Bantis	Asterios	IEM, International Hellenic University, Greece
3	Bardakas	A.	Institute of Nanoscience & Nanotechnology, NCSR Demokritos
4	Barrilet	Stani	FEMTO-ST, France
5	Bartasyte	Ausrine	Femto-ST, France
6	Bartsyte	Ausrine	Institut Universitaire de France, FEMTO-ST, France
7	Bechtsis	Dimitrios	IEM, International Hellenic University, Greece
8	Chatzimpaloglou	Alexandra	IEM, International Hellenic University, Greece
9	Costanza	Mario	FEMTO-ST, France
10	Dziuba	Anna	Poznan University of Technology, Poland
11	Gala	Georgia	IEM, International Hellenic University, Greece
12	Gauthier-Manuel	Ludovic	FEMTO-ST, France
13	Giuffrida	Giada	FEMTO-ST, France
14	Hatzopoulos	Argyrios T.	IEE, International Hellenic University, Greece
15	Intzes	I.	IEE, International Hellenic University, Greece
16	Iosifidou	Fani	IEM, International Hellenic University, Greece
17	Kantela	Katerina	IEM, International Hellenic University, Greece
18	Kapousizi	Dimitra	IEM, International Hellenic University, Greece
19	Karra	Fani	IEM, International Hellenic University, Greece
20	Karzi	Ioanna	IEM, International Hellenic University, Greece
21	Kennou	S.	Department of Chemical Engineering, University of Patras
22	Kiziroglou	Michail E.	IEM, International Hellenic University, Greece
23	Kochliaridis	Ippokratis	IEM, International Hellenic University, Greece
24	Kolla	Vilelmini-Maria	IEM, International Hellenic University, Greece
25	Kontaxi	Aikaterini	IEM, International Hellenic University, Greece
26	Kosmanis	Theodoros I.	IEM, International Hellenic University, Greece
27	Kostoula	Evanthia	IEM, International Hellenic University, Greece
28	Kotopoulou	Marina	IEM, International Hellenic University, Greece
29	Kotsani	Ifigeneia	IEM, International Hellenic University, Greece
30	Kouda	Ioanna	IEM, International Hellenic University, Greece
31	Kouderis	Nikolaos - Christos	IEM, International Hellenic University, Greece
32	Kouia	Despoina	IEM, International Hellenic University, Greece
33	Koumpakis	Dimitrios-Aristotelis	IEM, International Hellenic University, Greece
34	Koutsoudakis	George	Smiling Machines
35	Krokida	Eleni	IEM, International Hellenic University, Greece
36	Krontiras	C. A.	Department of Physics, University of Patras
37	Lagouda	Zoi	IEM, International Hellenic University, Greece
38	Lambois	Matthieu	FEMTO-ST, France
39	Leliopoulos	Vasileios	IEM, International Hellenic University, Greece
40	Liontou	Evaggelia	IEM, International Hellenic University, Greece
41	Louka	Kornilia	IEM, International Hellenic University, Greece
42	Margueron	Samuel	Femto-ST, France
43	Micard	Quentin	FEMTO-ST, France
44	Michailidou	M.	IEM, International Hellenic University, Greece
45	Michel	Gérard	FEMTO-ST, France

No	Last Name	First Name	Affiliation
46	Mindis	Ioannis	IEM, International Hellenic University, Greece
47	Moutafidis	Charis	Smiling Machines
48	Mpantias	Georgios	IEM, International Hellenic University, Greece
49	Nella	Anastasia	IEM, International Hellenic University, Greece
50	Nenos	Konstantinos	IEM, International Hellenic University, Greece
51	Nteni	Kornilia	IEM, International Hellenic University, Greece
52	Ouhabaz	Merieme	FEMTO-ST, France
53	Paliatsou	Anastasia	IEM, International Hellenic University, Greece
54	Papadopoulou	Maria S.	IEE, International Hellenic University, Greece
55	Papakostas	Dimitrios	IEE, International Hellenic University, Greece
56	Papanikolaou	Vagia	IEM, International Hellenic University, Greece
57	Segkos	A.	Institute of Nanoscience & Nanotechnolog , NCSR Demokritos
58	Sidiroglou	E.	IEE, International Hellenic University, Greece
59	Sidiropoulos	Vasileios	IEM, International Hellenic University, Greece
60	Teletos	E.	IEE, International Hellenic University, Greece
61	Terzis	Nikolaos	IEM, International Hellenic University, Greece
62	Toka	Aikaterini	IEM, International Hellenic University, Greece
63	Tsamis	Christos	Institute of Nanoscience & Nanotechnology, NCSR Demokritos
64	Tsiakmakis	K.	IEE, International Hellenic University, Greece
65	Tsioupros	S.	IEE, International Hellenic University, Greece
66	Tziourtzioumis	Dimitrios N.	IEM, International Hellenic University, Greece
67	Tzouna	Eleni	IEM, International Hellenic University, Greece
68	Vasileiou	Vasileios-Christos	IEM, International Hellenic University, Greece
69	Vassios	V. D.	IEE, International Hellenic University, Greece
70	Vekinis	G.	Institute of Nanoscience & Nanotechnology, NCSR Demokritos
71	Vellios	G.	IEE, International Hellenic University, Greece
72	Vlachos	Dimitrios	Department of Mechanical Engineering, AUTH
73	Voglitsis	Dionisis	Smiling Machines Ltd
74	Zafeiriadis	Dimitrios	MSc in Applied Automation Systems, IHU
75	Zaphiris	John	IEM, International Hellenic University, Greece
76	Zarogiannou	Eirini	MSc in Robotics, STEAM & New Technologies in Education, IHU
77	Zioga	Matina	IEM, International Hellenic University, Greece

Programme

08:45-09:00: Registration

Please check-in or register at the front desk.

09:00-09:05: Welcome and introduction

09:05-10:45: First Oral Session (Session Chair: Eirini Aivazidou, IHU)

09:05-10:00: Designing $LiNbO_3$ lead free-materials for energy harvesting with stable performances, *Samuel Margueron, Femto-ST, France,* 23WOM-01 (Invited)

10:00 Hybrid Deep Learning Models for Predictive Maintenance. *G. Koutsoudakis and Ch. Moutafidis*, *Smiling Machines Ltd*, 23WOM-02

10:15: Pseudo-Random Number Generator Implementation with Linear Feed Shift Register Circuits at Distinct Clock Frequencies, *S. Tsioupros, E. Sidiroglou, G. Vellios, I. Intzes and D. Papakostas*, 23WOM-03

10:30: Soil Electrical Conductivity Measurement, *E. Teletos, K. Tsiakmakis and A. T. Hatzopoulos*, 23WOM-04

10:45-11:15: Coffee Break and Poster Session (Session Chair: Kiziroglou Michail (IHU)

P1. VR Training Application for AR-Assisted Logistics Operations, *V. C. Vasileiou, D. Bechtsis, V. Sidiropoulos and D. Vlachos*, 23WOM-05.

P2. Is Warm-Up Necessary? – Instrument Performance Verification Test, *V. D Vassios., A. T. Hatzopoulos, K. Tsiakmakis and M. S. Papadopoulou*, 23WOM-06

P3. Theoretical Model of Acoustic Power Transfer through solids, *I. Kochliaridis and M. E. Kiziroglou*, 23WOM-07

P4. Development of a Customized Prototyping board for the PN7160 Near Field Communication Microchip, *A. Chatzimpaloglou and M. E. Kiziroglou*, 23WOM-08

11:15-12:15: Second Oral Session (Session Chair: Argyris Hatzopoulos, IHU)

11:15-12:00: Triboelectric energy harvesting for autonomous electronic devices, *C. Tsamis,* 23WOM-09.

12:00: Further Evaluation and Calibration of a Mie Scattering-based Apparatus for Portable Optical Haematological Analysis, *A. Bantis, M. Michailidou and A. Dziuba*, 23WOM-10.

12:15: Remotely Operated Vehicles as a Means of Training Higher education Students in Underwater Surveying, *T. Anagnostaki, D. Tziourtzioumis and Th. Kosmanis*, 23WOM-11

12:30: Utilization of fermentable biomass for bioethanol production and design of sustainable modular energy storage liquid fuel unit, *D. A. Koumpakis and D. Tziourtzioumis*, 23WOM-12.

12:45-13:15: Best Paper Award by Ioannidis Electronics. Concluding remarks.

13:30 Third Oral Session: **Erasmus Perspectives in Primary and Secondary Education**
(Session Chair: Dr. Theodoros Kosmanis, IHU. Session Co-Chairs: Dr. Dimistrios Tziourtzioumis, IHU, Dr. Vagia Papanikolaou, IHU)

13:30: Green Spark, *D. Kapousizi, K. Kantela, F. Karra, Z. Lagouda, I. Mindis, A. Nella and A. Paliatsou*, 23WOM-13

13:45 Design Thinking, *I. Karzi, M. Kotopoulou, I. Kotsani, I. Kouda, D. Kouia and E. Krokida*, 23WOM-14

14:00 Epi-STEAM-moniko School, *A. Kontaxi, N. Ch. Kouderis, V. Leliopoulos, E. Liontou. G. Mpantias and K. Nenos*, 23WOM-15

14:15 Smart Recycling, *F. Iosifidou, A. Toka and E. Zarogiannou*, 23WOM-16

14:30 Make it Gree, *V. M. Kolla, G..Gala, M. Zioga, E. Kostoula, K. Louka, N. Terzis and E. Tzouna*, 23WOM-17

14:45 Music Mode, *K. Nteni*, 23WOM-18

WORKSHOP PAPERS

*Note: The papers from 23WOM12 to 23WOM-16 will be added
to the proceedings after the conference.*

Designing LiNbO₃ lead free-materials for energy harvesting with stable performances

Samuel MARGUERON[1,*], Merieme OUHABAZ[1], Giada GIUFFRIDA[1], Matthieu LAMBOIS[1], Stani BARRILET[1], Gérard MICHEL[1], Ludovic GAUTHIER-MANUEL[1], Mario COSTANZA[1], Quentin MICARD[1], Ausrine BARTSYTE[1,2]

[1] Institut FEMTO-ST, UBFC, CNRS, UFC, ENSMM, 15B avenue des Montboucons Besançon, France
[2] Institut Universitaire de France

Corresponding author e-mail: Samuel.margueron@femto-st.fr

Abstract— **Bending cantilevers made of metal and LiNbO₃ for energy harvesters present one of the best figures of merit among lead-free piezoelectric materials, with wide industrial availability. However, the stability in frequency of the cantilever depends on the composite properties under varying environmental conditions. Moreover, fatigue upon actuation is critical for long-term battery replacement. In this presentation, the investigation of temperature stability, as well as the lifetime of LiNbO₃/metal harvesters, is conducted following several MEMS standards.**

Keywords—lead-free piezoelectrics, energy harvesting, metal MEMS, lifetime, structural strength

I. INTRODUCTION

Piezoelectric energy harvesting devices offer an appealing microsource of energy to power ultra-low consumption electronics and IoT [1,2]. The performance of the vibrating harvester depends on the electromechanical coupling of the piezoelectric material and the design of the cantilever structures [3] [4]. As most harvesters are made of lead based piezoelectrics (PZT), they suffer from fatigue, creep and depolarization [5]. Lead-free piezoelectric LiNbO₃ presents as good electromechanical coupling as PZT [6]; moreover, it can be found commercially in inexpensive single crystal wafers that should not suffer from fatigue. LiNbO₃ can be bonded to multiple substrates, offering a variety of energy harvesting applications that depend on both material properties [7]. However, for stable frequency applications, one has to validate long-term performance as well as the stable frequency of operation. In the present work, thermal modeling and experimental testing following MEMS standards are conducted to assess the structural strength and the influence of environmental conditions on the lifetime and stability of LiNbO₃ piezoelectric composites on metal substrates.

II. MATERIAL DESIGN

Unimorph and bimorph lithium niobate on metal substrates were produced by gold-gold bonding compression. Metal substrates were obtained from rolled stainless steel shims, 75 μm thick, cut into 4-inch discs, and polished. To improve surface quality, a 1 μm thick aluminum layer was sputtered onto the surface at room temperature and then repolished to a mirror finish [8]. 4-inch wafers of YX128° of LiNbO₃ were then coated with Cr and Au thin layers (15 nm/150 nm) and immediately bonded using a wafer bonder EVG501 at room temperature. The LiNbO₃ side was then thinned down to the desired thickness. Finally, the top electrode of Cr/Au (15 nm/150 nm) was deposited and cut into cantilever beams.

Among metal substrates, two families were evaluated: stainless steel 420 and 330. Alloy 330 is an austenitic nickel-iron-chromium alloy with excellent thermal properties, while alloy 420 is martensitic with chromium, providing corrosion resistance. The variations of the Young modulus as a function of temperature are given in Fig. 1, as well as the c_{11} of LiNbO₃ with temperature [9]. The coefficients of thermal expansion are approximately 10, 13.8, and 14 μm/m near room temperature for alloy 420, 330, and Z-LiNbO₃, respectively.
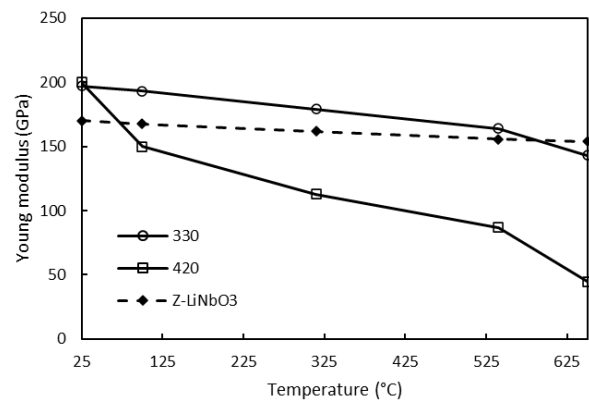

Fig. 1 Young modulus of Stainless Steel 420, 330 and LiNbO₃ (c_{11})

III. TEMPRATURE COEFFCIENT OF FREQUENCY

To evaluate the temperature coefficients of frequency in the range of standard temperatures (-50°C to 100°C), symmetrical bimorph beams made of LiNbO₃/metal/LiNbO₃ were considered in this section, so that thermal expansion can be neglected at first order. The variations of Young modulus of stainless steel and LiNbO₃ were interpolated to -50°C using linear regression from Fig. 1.
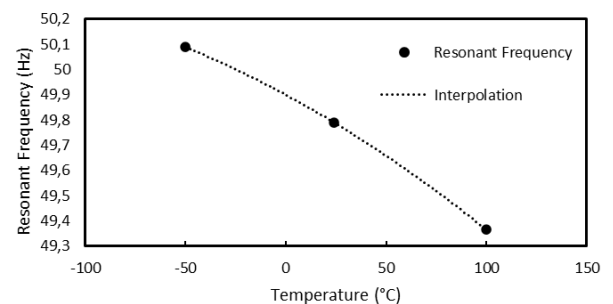
Fig. 2 Bending resonant frequency near 50 Hz of LiNbO₃ bimorph with alloy 330 as a function of temperature.

Fig. 2 reproduces the FEM calculation of the bending resonant frequency at -50, 25, and 100°C for a bimorph structure of LiNbO₃/alloy330/LiNbO₃ (50 μm/70 μm/50 μm). The length and resonant frequency were optimized close to 50 Hz. The three data points are interpolated for guidance. The preliminary results show a frequency stability of less than 1

Hz over -50 to 100°C for alloy 330. Current investigations are being conducted on other metal alloys and thicknesses. One can conclude from this investigation that it is possible to define a bimorph structure that fulfills the specifications of a temperature-stable harvester. Meanwhile, the drift in frequency can also occur from material fatigue.

IV. FATIQUE TESTING

Fatigue testing was conducted according to standard NF EN 62047-12 to assess the response under a large number of cycles (up to 10^8) in a short time. The samples were subjected to a sinusoidal electric excitation at the resonant frequency of 1 kHz. The cantilever beam tests were performed on unimorph samples with 75 μm of stainless steel and 50 μm of LiNbO$_3$, a width of 10 mm, and a length of 11 mm clamped on a PCB board. The electric fatigue tests are plotted in Fig. 3 with RMS electrical potential of 2.5V, 10V, and 20V. The figure presents the ratio of the resonant frequency normalized to the initial resonant frequency. It can be noted that for low electrical field, the frequency varies by less than 1%, whereas for high electric field, the frequency can vary up to 5% at 10^8 cycles. The softening of the resonance frequency can originate from clamping degradation as well as internal sample modification. No changes were observed optically, as well as on the static impedance of the samples, which seems to indicate that the frequency stability may primarily depend on the clamping with time. This conclusion is also motivated by the high stresses developed in the clamping [10]. To power an IoT device, a minimum of 3 V should be provided to the electronic board [2], and it is possible that the current clamping meets these specifications. Meanwhile, one must evaluate the maximum stresses that can be tolerated at the clamping.
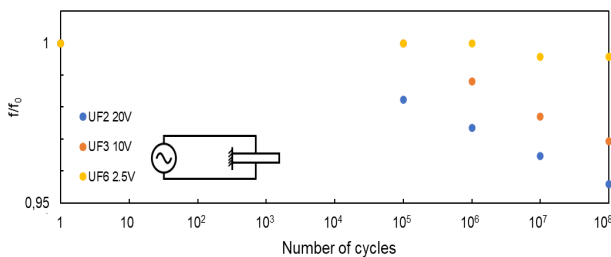

Fig. 3 Variation of the resonant frequency at 1 kHz on unimorph samples after electrical fatigue test at 2.5, 10 and 20 V$_{rms}$

V. BENDING STRENGTH

The bending strength of LiNbO$_3$/SS uniform was assessed following the ASTM D790-03 standard. The composites were tested under three-points bending tests. The test was conducted with a 20 N load cell by applying a maximum displacement of 2 mm at the mid-point of 5 mm x 30 mm beams at a loading rate of 0.01 mm/s in a controlled environment (T=23°C, RH%=50). The maximum stress is concentrated on the tensile loaded side nearly opposite to the central force position. Flexural tests were performed under displacement control. The strength distributions for three batches are represented in the Weibull diagram with 60 samples. The corresponding Weibull parameters σ0 and the Weibull modulus were evaluated using the EN 843 5 standard. The tensile strength values of LiNbO$_3$ films are summarized in table 1. The characteristic strengths are 74.8, 60.0, and 64.6 MPa for the uniform beam. It can be noted that the three batches of samples were prepared with different

polishing of the top surface, which explains the variation in flexural strength. One can then conclude that the strength of the harvester made of single crystalline LiNbO$_3$ depends on the surface quality of polishing, which is the locus of fracture under tensile testing.

TABLE I.   BENDING STRENGTH

Sample batch	Flexural Strength			
	Average (MPa)	*Lower (MPa)*	*Upper (MPa)*	*Standart de. (MPa)*
#1	70.65	52.06	89.82	10.24
# 2	55.66	35.07	74.66	11.47
# 3	60.80	41.11	82.49	9.67

VI. . CONCLUSION

The experiments and theoretical work were conducted on LiNbO$_3$ piezoelectric devices bonded to stainless steel. We demonstrate that among various materials, certain metal alloys can exhibit low temperature coefficients of frequency. However, the degradation of cantilever harvester composites made of brittle LiNbO$_3$ shows scattered strengths that depend on the variability of size and location of defects in individual specimens. This issue is further exacerbated when considering the clamping, which should be a concern for LiNbO$_3$/metal harvesters in terms of resonance quality as well as long-term stability.

ACKNOWLEDGMENT

REFERENCES

[1]   H. Li, C. Tian, and Z. D. Deng, "Energy harvesting from low frequency applications using piezoelectric materials", Appl. Phys. Rev. 1, 041301, 2014.

[2]   N. Panayanthatta and al., "A Self-Powered and Battery-Free Vibrational Energy to Time Converter for Wireless Vibration Monitoring", Sensors 21(22):7503, 2021.

[3]   A Erturk and D J Inman, "An experimentally validated bimorph cantilever model for piezoelectric energy harvesting from base excitations", Smart Mater. Struct. 18 025009, 2009.

[4]   K. M. Mossi, G. V. Selby and R. G. Bryant, "Thin-layer composite unimorph ferroelectric driver and sensor properties", Materials Letters 35, 39–49, 1998.

[5]   K. Okazaki and T. Tanimoto, "Electro-mechanical strength and fatigue of ferroelectric ceramics", Ferroelectrics, 131:1, 25-40, 1992.

[6]   A. Bartasyte and al., "Material strategies to enhance the performance of piezoelectric energy harvesters based on lead-free materials", J. Micromech. Microeng. 33 053001, 2023.

[7]   G. Clementi and al., "LiNbO3 films – A low-cost alternative lead-free piezoelectric material for vibrational energy harvesters", Mechanical Systems and Signal Processing, 149(12), 107171, 2021.

[8]   Patent EP20 203952 (10/2020), "Piezoelectric device comprising flexible single crystalline piezoelectric LiNbO3 and/or LiTaO3 films integrated on flexible substrate and methods for producing the same A. Bartasyte, S. Margueron, F. Bassignot, L. Gauthier-Manuel, G. Clementi, M. Ouhabaz

[9]   H. de Castilla, P. Bélanger and R. J. Zednik, "High temperature characterization of piezoelectric lithium niobate using electrochemical impedance spectroscopy resonance method", J. Appl. Physic. 122, 244103, 2017.

[10]   J.A. Brans, T.W.A. Blad and N. Tolou, "A Review of Design Principles for Improved Mechanical Reliability of CantileverPiezoelectric Vibration Energy Harvesters", 7th International Conference on Control, Mechatronics and Automation (ICCMA), 2019.

Hybrid Deep Learning Models for Predictive Maintenance
George Koutsoudakis and Charalampos Moutafidis
Smiling Machines Ltd, Greece

The adoption of machine learning and deep learning methodologies in the predictive maintenance of motor bearings presents a transformative potential for industrial operations. The research conducted by Smiling Machines introduces a cutting-edge approach that utilizes a hybrid model, combining Convolutional Neural Networks (CNNs) and Recurrent Neural Networks (RNNs), to anticipate maintenance requirements. Detailing the implementation and advantages of the integrated model over traditional singular network approaches.

In practice, Smiling Machines has equipped numerous industrial settings with advanced sensors, facilitating extensive data acquisition for model training within a robust cloud infrastructure. This initiative has yielded substantial datasets, providing a foundation for the hybrid model's development and refinement. The model's architecture merges CNN's prowess in spatial feature detection with RNN's temporal data sequencing to outperform standard models in failure prediction accuracy.

Additionally, the presentation introduces the Learning from Mistakes Algorithm (LEMA), an AI methodology inspired by human learning patterns, particularly the ability to learn from errors. This novel addition has shown promise in emulating complex problem-solving skills within the AI framework, enhancing the model's predictive capabilities through iterative learning and adaptation.

The cloud infrastructure designed by Smiling Machines plays a pivotal role in the predictive maintenance ecosystem for motor bearings. The architecture is engineered to handle vast streams of sensor data, seamlessly facilitating real-time data processing and storage. It serves as the backbone for the deployment of the hybrid deep learning models, ensuring robustness, scalability, and high availability. In our presentation, we will provide an in-depth analysis of the cloud infrastructure's design, its integration with our predictive models, and how it enhances our system's overall performance and reliability.

Pseudo-Random Number Generator Implementation with Linear Feed Shift Register Circuits at Distinct Clock Frequencies

S. C. Tsioupros, E. C. Sidiroglou, G. D. Vellios, I. G. Intzes, D. K. Papakostas

International Hellenic University, Department of Information and Electronic Engineering
Thessaloniki, Greece

Abstract— **Pseudorandom Number Generators (PRNGs) play a vital role in various fields, from cryptography to simulations and microsystem applications. This paper presents an innovative approach to PRNG implementation, contributing to the theory and applications of a complex PRNG based on a circuit with 2 LFSRs (Linear Feedback Shift Registers) in different clock frequencies. A thorough overview of the circuit's essential parts is provided, and the main concept of this study is introduced, covering both the theory and the practical application of the circuit. Furthermore, the simulation of PRNG and the experimental validation is conducted through MATLAB and Verilog implementation respectively, with corresponding comparisons. Subsequently, the study evaluates the performance of PRNG systems when using multiple LFSRs compared to systems with just one LFSR. Prospective extensions are also considered, highlighting future directions in the sphere of ASIC fabrication.**

Index Terms—**Digital Circuits, PRNG, LFSR, Tiny Tape Out, ASIC**

I. INTRODUCTION

In the dynamic realm of electronics, where creativity is essential, the advancement of digital circuits demonstrates the continuous endeavor to augment effectiveness and dependability. Central to this progress is the fascinating domain of Pseudorandom Number Generators (PRNGs), crucial in shaping today's digital systems. PRNGs, by their very nature, generate sequences of numbers that mimic the properties of truly random sequences. However, unlike truly random sources which rely on physical processes for entropy, PRNGs operate deterministically, driven by an initial seed value [1]. The primary objective of this endeavor is to present an innovative approach to PRNG implementation, shedding light on a circuit architecture leveraging two Linear Feedback Shift Registers (LFSRs) operating at distinct clock frequencies. This not only enriches the generation of pseudorandom sequences but also introduces a novel dimension to the traditional understanding of PRNG systems. This project was pursued in response to the opportunities provided by Tiny Tape Out, an educational initiative that enables a more accessible and cost-effective process for manufacturing real semiconductor chips from digital designs.

In the following sections, the theoretical intricacies of the proposed PRNG system are delved into, the practical aspects are explored through simulations and hardware implementation, and its performance is critically evaluated against conventional PRNGs. Through this journey, valuable insights are aimed to be contributed to the ongoing dialogue on the evolution of electronics and the integral role of PRNGs in shaping the landscape of digital systems.

II. THEORETICAL FRAMEWORK

It is deemed necessary to explain the fundamental elements and technologies that the project is based on.

A. Field-Programmable Gate Array (FPGA)

FPGA is a highly versatile integrated circuit characterized by its post-manufacturing configurability. It allows users to customize internal circuitry, employing logic elements such as Look-Up Tables (LUTs) and flip-flops. These elements can be reconfigured using Hardware Description Languages (HDLs) such as Verilog or VHDL, providing designers with a high degree of flexibility. With its exceptional parallel processing capabilities, this technology can execute multiple operations at the same time, which makes it ideal for real-time applications in a variety of industries, such as aerospace, medical devices, automotive electronics, and telecommunications. Its adaptability extends to the implementation of diverse digital circuits, from simple combinational logic to intricate digital systems. The high processing speed further enhances its utility, especially in applications where rapid response times are critical. One of the key advantages of FPGAs is their re-programmability [2]. This feature allows designers to iteratively refine and test their designs, making them valuable in scenarios where design requirements may evolve or change over time.

B. Application-Specific Integrated Circuit (ASIC)

In the world of integrated circuits, the Application-Specific

Integrated Circuit stands out as a highly specialized semiconductor with a fixed functionality tailored for specific applications. ASICs are known for their meticulous engineering, which optimizes their physical size, power consumption, and performance for specific use cases. To fabricate the integrated circuit on a silicon wafer, the manufacturing process involves intricate procedures such as photolithography and etching. Customization allows designers to include essential components, maximizing efficiency. In some applications ASICs outperform FPGAs and general-purpose processors in terms of performance [3,4]. Integration prowess enables multiple functions on a single chip, simplifying system design and enhancing reliability. Despite high development costs, ASICs find applications in telecommunications, automotive electronics, consumer electronics, and medical devices. ASICs provide a fixed yet highly optimized solution for stable requirements, contrasting with the re-programmability of FPGAs, offering adaptability and customization.

C. Linear Feedback Shift Register (LFSR)

LFSR is a specialized shift register that distinguishes itself by incorporating a feedback mechanism based on linear functions. Within its structure, the shift register consists of flip-flops organized in a chain, where each flip-flop stores a single bit of data (Fig. 1). On each clock cycle, the bits are shifted to the subsequent flip-flop. The uniqueness of this digital circuit lies in its feedback process. One or more outputs from the flip-flops are fed back into the input, and the specific outputs involved are determined by a linear feedback function, often represented as an XOR (Exclusive OR) operation [5]. This feedback mechanism introduces a dynamic element to the register, influencing the sequence of bits generated. The operation of an LFSR is regulated by a clock, defining the frequency at which the bits shift, and the feedback occurs. The result is a sequence of binary values that appears pseudorandom, offering applications in cryptography and error correction [6]. In practical terms, LFSRs are valuable tools for generating pseudorandom sequences due to their deterministic yet seemingly random output. They find applications in encryption algorithms, stream ciphers, and error detection and correction protocols.
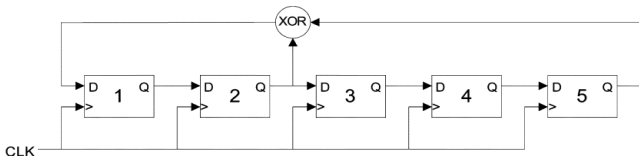

Fig. 1. Schematic description of a 5-bit LFSR [5].

D. Multiplexers (MUXes)

MUXes are specialized digital circuits designed to selectively route data from multiple input sources to a single output. Consisting of multiple data input lines, a control input, and a single output line, a MUX operates based on the control input, determining which data input is transmitted to the output. The selection of a specific input is often governed by a binary code on the control input, activating the corresponding data line. MUXes are highly versatile and find applications in various digital systems, serving functions such as data routing and signal selection. Their efficiency lies in the ability to streamline data paths and reduce the complexity of circuitry, enhancing overall system performance. MUXes play a crucial role in applications like data multiplexing, communication systems, and arithmetic logic units within processors [7,8]. Their adaptability and simplicity make them fundamental components in digital design, offering efficient solutions for managing data flow and signal routing in electronic systems.

For this project two LFSRs were used, each having its output fed into a 2:1 multiplexer to increase the randomness of the output bits. The 16-bit LFSR for the input bit and the 8-bit LFSR for the selection bit of the 16-to-8 multiplexer.

III. SIMULATION

The theoretical analysis section offered a deep understanding of the principles underlying the operation of the circuit with the LFSR (Linear Feedback Shift Register) at different frequencies, and how accomplishes to generate pseudorandom numbers. Transitioning from theory to practical implementation, initially it is crucial to focus on the intermediate point: the simulation of the system. This simulation will allow to evaluate the behavior of the circuit and its effect on the signal in the time domain.

During this module, a simulation using the MATLAB programming language will be performed by defining the circuit parameters, -including the initial values and the different operating frequencies of each LFSR- running the simulation and evaluating the results, observing how frequency affects the behavior of the LFSR and the time-domain effect. As a result, a comprehensive understanding will be achieved of how the LFSR can be used to generate signals at different frequencies and evaluate the effects of the parameters that were chosen. The schematic design of the project idea is shown in figure 2.
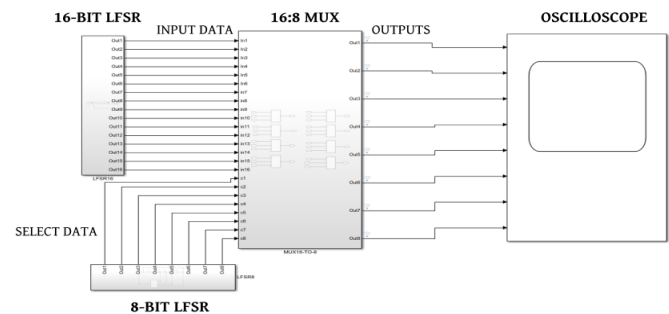

Fig. 2. Schematic illustration from PRNG circuit in Simulink.

It will be observed that the outputs from the multiplexer are identical, just shifted by some time units (Fig. 3). Importantly, the outputs of this block are the 16th degree polynomial of the 16bit LFSR, so this phenomenon is justified. Subsequently, it becomes evident that when the same clock frequency is utilized in both LFSRs, there is a slower output in one, while with the clock frequency of the 8-bit LFSR being twice that of the other, the outputs are significantly greater. This discrepancy is attributed to the faster sampling that has been implemented.

$$P(x) = x^{16} + x^{15} + x^{14} + x^{13} + x^{12} + \cdots + x^1 + 1$$

For the 8-bit LFSR the coefficients 8 6 5 4 were chosen and for the 16-bit LFSR the coefficients 16 15 14 4, both using nxor gates in feedback.
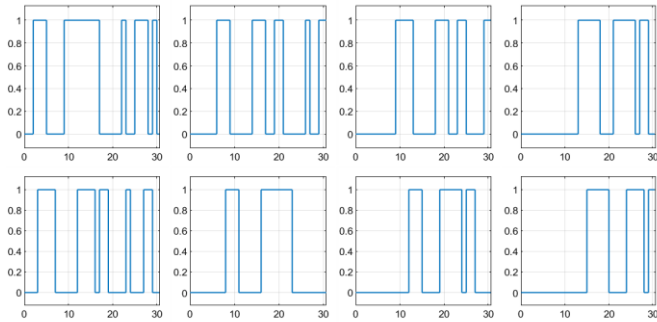

Fig. 3. Waveforms at same clock frequency

In the attempt to perform a simulation with a programming language, the examination of the building blocks of our circuit from the perspective of Python was an interesting aspect. PyLFSR is an open-source Python library designed for the creation of Pseudo-Random Generators based on Linear Feedback Shift Registers. The generated sequences can undergo testing for various properties. Consequently, the PyLFSR library facilitates tasks such as autocorrelation analysis and more, expanding the toolkit available for such analyses.

Autocorrelation refers to the correlation of a signal with a copy of itself. The analysis of autocorrelation involves a mathematical process aimed at identifying repeating patterns, especially in scenarios where a periodic signal might be obscured by noise. LFSRs are widely used for generating random number sequences with very good correlation properties. It is established that, with a suitable selection of feedback coefficients [9], an LFSR with L cells produces a sequence of length $N=2^L-1$, featuring out-of-phase autocorrelation values $R(\tau)=-1$ for any non-zero shift $1 \leq \tau \leq N-1$. Notably, considering the maximum autocorrelation value as $R(0)=N$, the behavior of these sequences, particularly for large N, closely resembles that of ideal sequences, as discussed by the authors in [9], where $R(\tau)=0$ for any non-zero shift. Autocorrelation functions with great randomness are shown in figure 5 and 6 while in figure 4 a noticeable lack of beneficial randomness is evident.
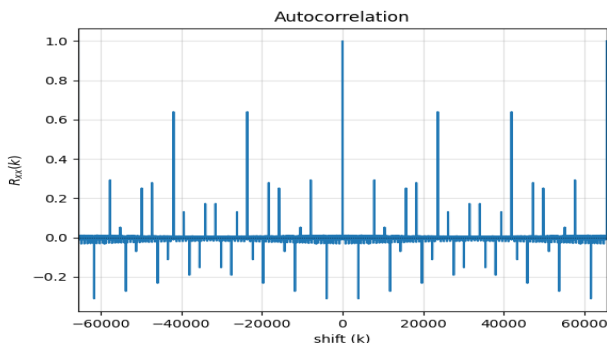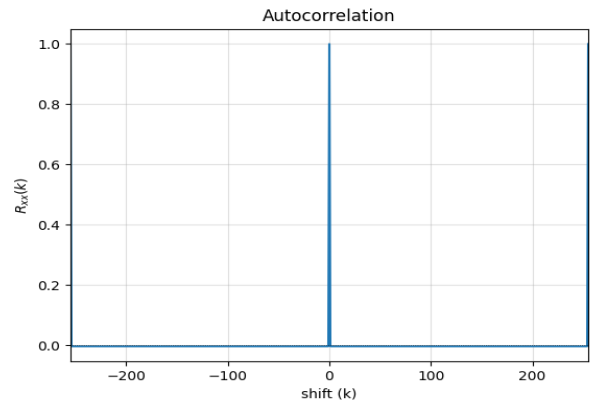

Fig. 4. Autocorrelation of 16-bit LFSR.

Fig. 5. Autocorrelation of 8-bit LFSR.

When comparing the designed circuit with a simple PRNG featuring a 4-bit LFSR, several advantages are observed. The increased complexity of the system introduces greater randomness to the final results, expanding the range of possible combinations. Numbers up to the binary value of 1111 can be generated by a 4-bit LFSR, with a periodicity of 15 clock cycles. In contrast, the system we present utilizes a maximum 16-bit LFSR, capable of reaching up to the value 11111111 11111111, with a significantly longer periodicity of 65535 clock cycles.
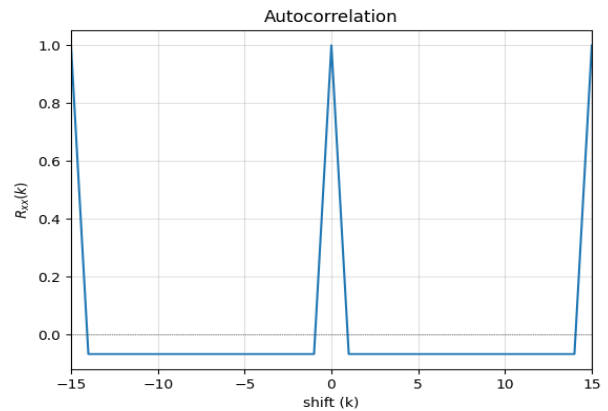

Fig. 6. Autocorrelation of 4-bit LFSR.

Nevertheless, there are drawbacks associated with our system's increased complexity, such as higher power consumption, increased computational demands, and greater space utilization compared to a simple LFSR. In its entirety, our circuit necessitates a total of 455 cells on a single chip.

IV. EXPERIMENTAL PROCEDURE

It is deemed necessary to explain the fundamental elements and technologies that the project is based on.

A. Development Board

The DE1-SoC Development Kit was utilized for our project, a robust and flexible platform crafted by Terasic Inc (Fig.7). Significantly contributing to this project, this development board featured a Cyclone V SoC FPGA from Intel, integrating a dual-core ARM Cortex-A9 processor with FPGA fabric. A

rich array of peripherals, interfaces, and connectivity options is boasted by the kit, providing a conducive environment for digital design exploration and embedded systems development. The FPGA's re-programmability was utilized to implement custom digital circuits, while the execution of embedded software was facilitated by the ARM processor. DE1-SoC served as an invaluable tool, offering seamlessly hardware integration, making it an ideal choice for accomplishing this idea.
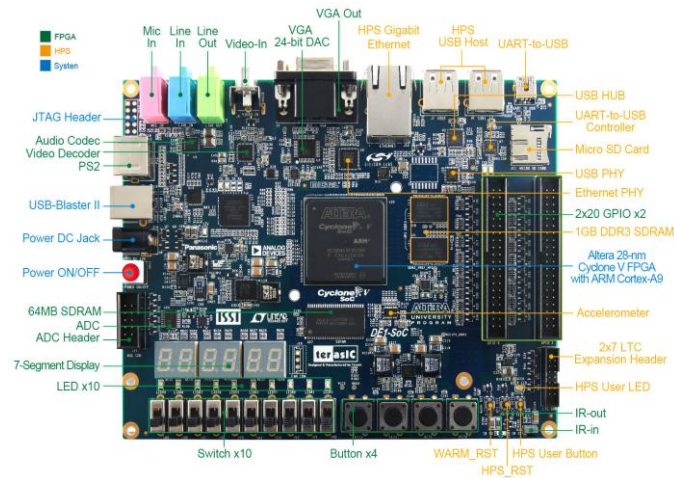

Fig. 7. DE1-SoC Development Kit [10].

B.   Quartus II

Quartus II, now known as Intel Quartus Prime, is a powerful design tool tailored for programmable logic devices. This tool served as a comprehensive platform for the HDL designs. It offered capabilities such as analysis and synthesis of designs, project compilation, RTL diagram visualization, hardware description through Verilog, and intuitive visual editing of logic circuits. implementation of digital systems. The collaborative utilization of Intel Quartus Prime and DE1-SoC played a crucial role in the success of the project, providing a robust framework for the development and implementation of digital circuits.

C.   Code

Verilog, a hardware description language, played a crucial role in the execution of this idea. For the generation of pseudo-random sequences two LFSRs modules were implemented, one operating with an 8-bit configuration and the other with a 16-bit configuration. The circuit, driven solely by a clock signal and an enable pin, had no input data but produced output on two 7-segment displays, involving a total of 14 output pins. Specifically, the 16-bit LFSR generated input for the 16-to-8 multiplexer module, while the 8-bit LFSR determined the selection bits for the same multiplexer. The 16-to-8 multiplexer module was implemented through the integration of eight 2-to-1 multiplexers. In the final stage of the circuit, the data underwent conversion into Binary-Coded Decimal (BCD) format, displaying the results on two 7-segment displays in hexadecimal format (Fig. 8). Verilog provided the language framework essential for expressing and realizing these intricate hardware functionalities.

Hexadecimal Value	Binary Value	Decimal Value
01	0000 0001	1
03	0000 0011	3
06	0000 0110	6
0C	0000 1100	12
0D	0000 1101	13
19	0001 0011	19

Fig. 8. Some of the output values of the two 7-segment displays.

V.   FUTURE WORK

The motivation behind this endeavor was to eventually implement the circuit in an Application-Specific Integrated Circuit (ASIC). As a preliminary step, the initial device implementation took place in an FPGA. Following thorough testing, the design was submitted for fabrication through the Tiny Tapeout program [11]. Anticipating the chip's delivery in approximately a year, our future efforts will focus on assessing the functionality of what was conceptualized, simulated in SIMULINK, and implemented in FPGA at the micrometer level within the ASIC domain. The space occupied by the circuit is shown in figure 9.
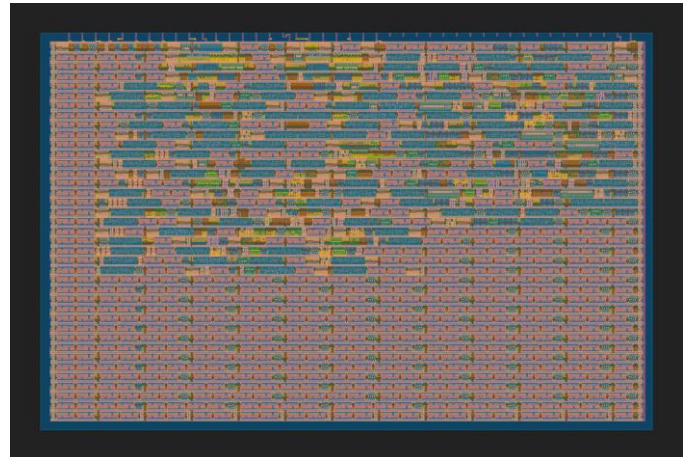

Fig. 9. Illustration of the 2Dimensional layout of the circuit.

VI.   CONCLUSION

The essential role that technology has by featuring two distinct Linear Feedback Shift Register (LFSR) blocks—one operating with 16 bits and the other with 8 bits, functioning at different clock frequencies—stands as a sophisticated pseudo-random number generator with wide-ranging applications. Leveraging an Application-Specific Integrated Circuit (ASIC) enhances the circuit's performance and energy efficiency. This circuit's pseudo-random number generation finds utility in diverse fields such as simulations, telecommunications, and cryptography. The adaptability of clock frequencies and LFSR length allows customization to meet the specific requirements of various applications. Notably, this circuit paves the way for future applications that necessitate highly dependable and efficient pseudo-random numbers, signifying the continual progress in randomization technology.

REFERENCES

[1] T. Tuncer, A. Erdinç, "Random number generation with LFSR based stream cipher algorithms," In 2017 40th International Convention on Information and Communication Technology, Electronics and Microelectronics (MIPRO), pp. 171-172, 2017.

[2] I. Masahiro, "What is an FPGA?," *Principles and Structures of FPGAs,* pp. 23-32, 2018.

[3] A. Amara, F. Amiel, T. Ea, "FPGA vs. ASIC for low power applications," *Microelectronics journal* 37.8, pp. 669-677, 2006

[4] D. Chinnery, K. Keutzer, "*Closing the gap between ASIC & custom: tools and techniques for high-performance ASIC design*," Springer Science & Business Media, 2002.

[5] R. S. Katti, R. Xiaoyu, K. Hareesh, "Multiple-output low-power linear feedback shift register design," *IEEE Transactions on Circuits and Systems I: Regular Papers* 53.7, pp. 1487-1488, 2006.

[6] M. Nilanjan, et al. "Ring generator: An ultimate linear feedback shift register." *Computer* 44.6, pp. 64-65, 2010.

[7] B. Malti, H. Singh, G. Sharma. "A taxonomical review of multiplexer designs for electronic circuits & devices," *Journal of Electronics and Informatics* 3.2, pp. 77-88, 2021.

[8] Y. P. Venkata, et al. "Dopingless transistor-based hybrid oscillator arbiter physical unclonable function." *2017 IEEE Computer Society Annual Symposium on VLSI (ISVLSI)*, pp. 609-611, 2017.

[9]   M. Baldi, F. Chiaraluce, N. Boujnah, and R. Garello, "Impact of truncation on the statistical properties of LFSR sequences," pp.1-4, 2009.

[10] Terasic, https://www.terasic.com (accessed December 15, 2023)

[11] Tiny Tapeout, https://tinytapeout.com/ (accessed November 13, 2023)

Soil Electrical Conductivity Measurement

Teletos E., Tsiakmakis K., Hatzopoulos A.T.

Department of Information and Electronic Engineering
International Hellenic University, Sindos, Thessaloniki, Greece

Abstract— **This work introduces a circuit that uses two metal electrodes set into the soil and op amps to measure the electric conductivity of soil. The circuit combines a full wave rectifier, floating current source, bipolar pulse generator, and conditioner to output a voltage between 0.5 and 5 V in relation to resistance. There are various reasons that soil electrical conductivity (EC) measurement is significant in the fields of geology, agriculture, and environmental research. The electrical conductivity of the soil is a metric that offers important insights into the physical and chemical characteristics of the soil. This experiment's primary objective is to evaluate EC, which is frequently used as a proxy for soil salinity and the presence of specific ions like nitrate. Experiments have been carried out for certain soil parameters, humidity, and temperature.**

Index Terms — **Circuit, Electric conductivity, Sensor**

I. Introduction

THE measurement of soil electrical conductivity (EC) is a fundamental aspect of understanding soil properties, crucial for optimizing agricultural yield and environmental assessments. Traditional EC measurement methods have ranged from direct current (DC) conductivity meters to more sophisticated approaches, each with unique advantages and inherent limitations [1].

For EC measurement, a common technique uses a voltage divider circuit with a pulsating mechanism. Although this method provides a simple strategy, it is not without drawbacks. By applying intermittent current instead of continuous current, corrosion is lessened, which is meant to minimize electrode exposure to ion-rich environments. However, some degree of electrode deterioration is unavoidable over time [2]. Because of the pulsing nature, a compromise must be struck between preventing corrosion and preserving accuracy, since even regulated pulsing can cause progressive wear of the electrodes.

To improve the accuracy of soil electrical conductivity testing, alternating current (AC)-based techniques based on sine wave production have been presented [3]. This approach, distinct from traditional methods, utilizes a continuous sine wave current to assess soil conductivity. The sine wave approach is useful in decreasing electrode polarization and ion deposition, both of which are major problems in DC-based systems. This leads in more consistent and accurate conductivity measurements. However, the use of sine wave techniques frequently involves a trade-off in terms of system complexity and operational costs, which may restrict their utility for routine soil testing.

The use of electromagnetic pulsed eddy currents is another notable approach. This technique, designed for quick and efficient soil conductivity surveys, requires a more complicated circuitry design in order to appropriately interpret transient signals [4]. While this approach decreases electrode corrosion, its complexity and the requirement for specialist equipment may make it too expensive for general usage in field situations.

Transitioning from electromagnetic techniques, the bipolar pulse method presents a different yet highly effective approach in reducing electrode corrosion for soil electrical conductivity measurements. This technique employs alternating positive and negative pulses with a low duty cycle, significantly minimizing the electrodes' exposure to corrosive conditions [5]. It effectively reduces electrode polarization and ion accumulation, which are common issues in continuous current methods. Despite offering superior corrosion protection, this method necessitates advanced signal processing to ensure accurate EC readings, thus achieving a balance between precision and electrode longevity.

This study introduces a soil electrical conductivity measurement method using the bipolar pulse principle. An operational amplifier (op-amp) generates a pulsed AC signal, leading into a voltage-to-current (V to I) converter under constant current conditions. The soil itself acts as the amplifying resistance, streamlining the system by removing the need for multiple resistors for calibration. This approach leverages the soil's resistivity as a variable component in the circuit. Voltage drops across the soil, influenced by its resistivity, are measured following Ohm's Law. The V to I converter's output, mirroring these resistivity changes, is processed through a full-wave rectifier, producing a DC voltage indicative of soil conductivity. Subsequently, this DC signal is stabilized and amplified, adjusting the voltage from 0.5V (high conductivity) to 5V (low conductivity). This method effectively merges the bipolar pulse approach with advanced circuitry, offering a compact and precise tool for real-time EC measurement, simplifying calibration and enhancing efficiency. The block diagram of setup used is shown in Fig.1.
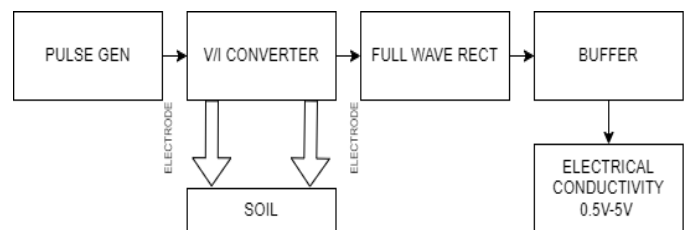

Fig. 1. Schematic description of the system concept.

II. Experimental Setup

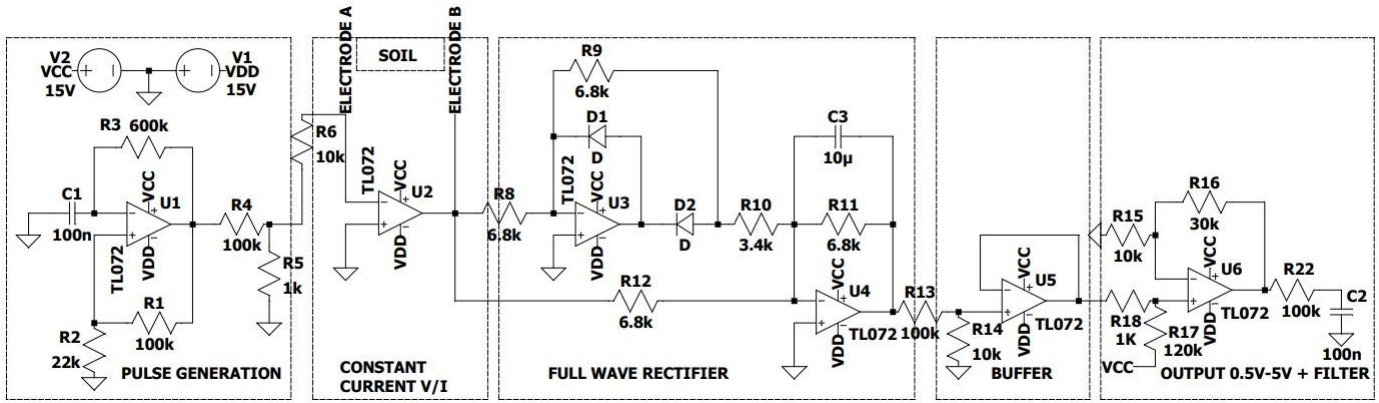This study presents a soil electrical conductivity

Fig. 2. Schematic of the Electrical Conductivity circuit.

measurement method, leveraging the bipolar pulse principle. At its core, an operational amplifier (op-amp) functions as an astable oscillator, generating a pulsed AC signal. The schematic of the Electrical Conductivity circuit is shown in Fig. 2. This signal is then directed into a voltage-to-current (V to I) converter, operating under constant current conditions. Significantly, the soil itself serves as the amplifying resistance in this setup. One of the pivotal design choices in this method is the elimination of the need for selecting different resistors for calibrating the output, simplifying the system considerably. This is achieved by utilizing the resistivity of the soil as a variable parameter within the circuit. The voltage drops across the soil, which varies with its resistivity, is measured in accordance with Ohm's Law. The output from the V to I converter, reflecting these resistivity changes, is then processed by a full-wave rectifier. This conversion yields a DC voltage that correlates directly with the soil's conductivity. Finally, the DC signal is first stabilized through a voltage divider and buffer, and then it undergoes amplification via another op-amp. This stage adjusts the voltage range from 0.5V, indicative of high conductivity (or low resistivity, approximately 0k to 3k ohms), to 5V, representing low conductivity (or high resistivity, in the range of 800k to 1 meg ohms). Thus, this method combines the bipolar pulse technique with an advanced circuit design, resulting in a compact, efficient, and precise tool for real-time soil EC measurement, while also reducing the complexity associated with calibration.

The system's suitability for field use allows for precise assessment of soil conditions. Future implementations could involve the use of Internet of Things (IoT) technologies, contributing significantly to the advancement of agricultural practices and the monitoring of environmental factors.

III. SIMULATION AND EXPERIMENTAL RESULTS

In this chapter simulation and experimental results are presented. The simulation results of pulse generated signal at input of the V to I block is shown in Fig.3.

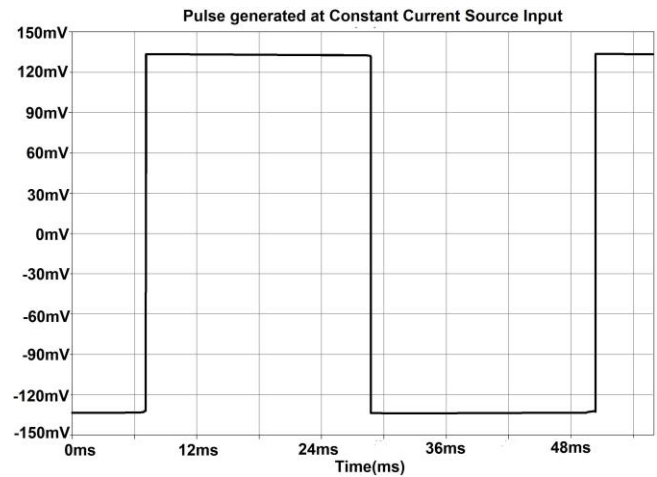Fig. 3. Simulation results of pulse generated signal at input of the V to I block
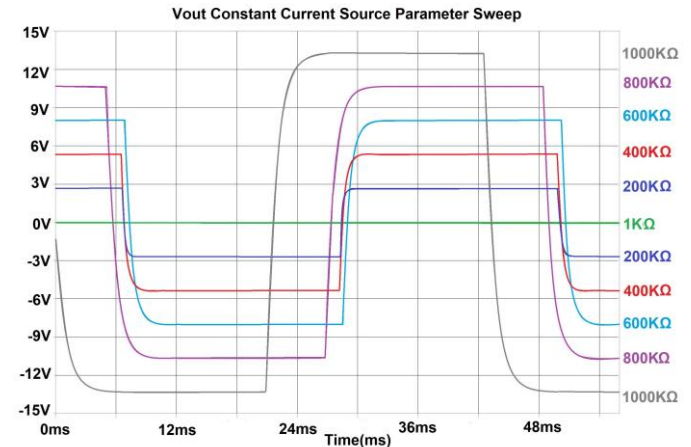

Fig. 4. Simulation results of the pulse that is being affected by the resistance of the soil ranging from 1kΩ to 1000kΩ

The simulation results relating the resistance between the electrodes and the voltage at the output of the circuit are shown in Fig.5. The relation between conductivity and output voltage appears to be linear.
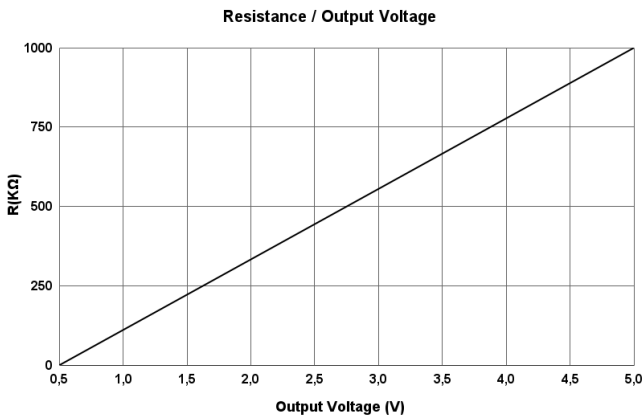
Fig. 5. Simulation results of resistance and voltage output of circuit. Conductivity from 1kΩ, 0.5V to 1MΩ, 4.7V.

Fig. 6 illustrates how the square pulse is distorted in relation to the actual measurement due to the capacitance exhibited by the soil. It demonstrates the variation of the voltage depending on the resistance of the soil. The sample of soil is dry.
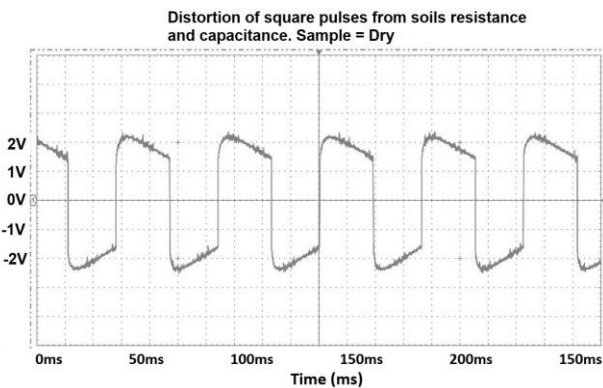

Fig. 6. Measurement obtained at the output of the second operational amplifier.

Fig. 7 graph illustrates how the square pulse is distorted in relation to the actual measurement due to the capacitance exhibited by the soil. It demonstrates the variation of the voltage depending on the resistance of the soil. This sample of soil is humid.
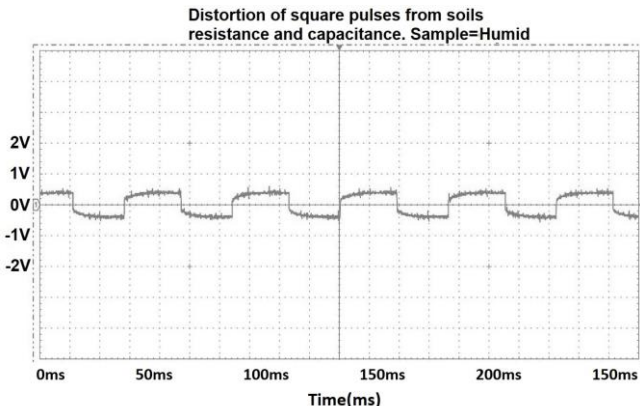

Fig. 7. Measurement obtained at the output of the second operational amplifier.

The output block measurement results indicate the voltage drift over time in semi-dry soil is presented in Fig.8.
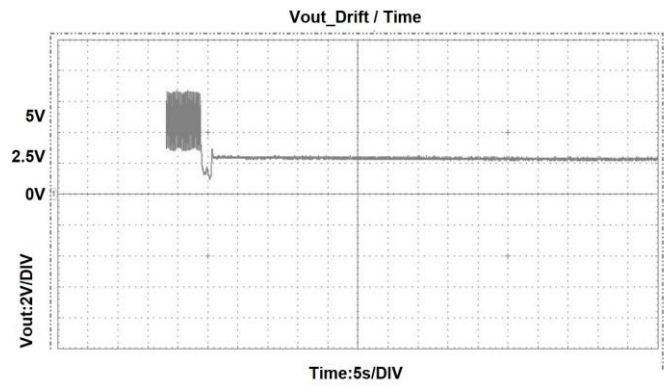

Fig.8. Measurement results of the output block showing the voltage drift over time in semi dry soil.
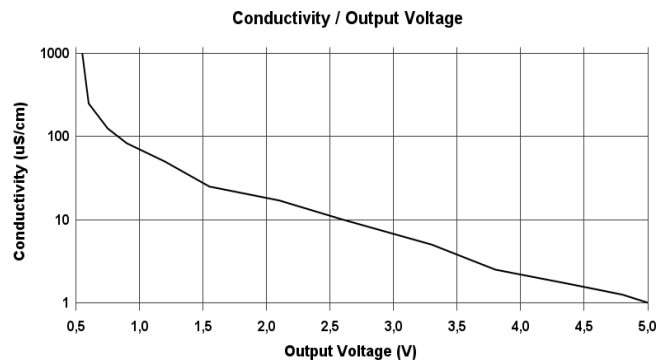

Fig.9. Measurement results of the output block showing the conductivity and voltage relation.

Fig.9 is useful for estimating conductivity by matching the output voltage to the corresponding point on the curve. This method is particularly valuable in a range of situations where voltage acts as a proxy for direct conductivity measurement.

For agricultural soils, the range of 1000μS/cm to 1μS/cm is sufficient to assess soil salinity levels, nutrient availability, and water content, which are critical for crop growth.

IV. CONCLUSION

Soil EC measurement is the first step to calculate some soil critical parameters for agriculture, like water content, salinity level and fertilization needs, which affect the plant roots neighborhood. The proposed method of this paper does not require to be carried out in a laboratory but can be done in the field, which is a clear advantage for the convenience and the time needed to be completed. In comparison with the AC sine wave production, our method uses alternating pulses to reduce the degradation of the electrodes and gives satisfactory results, without the need of different amplification resistors for different EC scales and can be directed straight to an ADC. The simulation results are close to the approximate measurements. Possible soil type analysis can be combined and give even closer measurements in this difficult area of soil parameter analysis and fertilization needs for yield improvement.

19

REFERENCES

[1] D. L. Corwin, S. M. Lesch, "Apparent soil electrical conductivity measurements in agriculture," *Computers and Electronics in Agriculture*, 1(46), pp. 11-43, 2005.

[2] M. I. Alif Muslan, W. F. H. Abdullah, Z. Zulkifli and A. B. Binti Rosli, "Electrical Conductivity Sensing Circuit Design Using Voltage Divider," *2022 IEEE 12th Symposium on Computer Applications & Industrial Electronics (ISCAIE)*, Penang, Malaysia, pp. 186-190, 2022.

[3] H. Lin, C. Cao, P. Xu, Y. Cai, Y. Ye and Y. Cheng, "Design of Electrical Conductivity Measuring Device Based on STM32," *2nd International Symposium on Control Engineering and Robotics (ISCER)*, Hangzhou, China, pp. 149-152, 2023.

[4] Zhu, Wenyue & Zhang, Lin & Peng, Yaping & Zhang, Qi & Gao, Mingchao & Fu, Yingchun, "Principle Analysis of Soil Electrical Conductivity Test Based on Pulsed Eddy Current," *IOP Conference Series: Earth and Environmental Science,* Vol. 242, No. 4, 2019.

[5] Yaoguang Wei, Jianqing Wang, Daoliang Li, Qisheng Ding, "Design of Intelligent Conductivity Meter Based on MSP430F149," *Third IFIP TC 12 International Conference on Computer and Computing Technologies in Agriculture III (CCTA)*, Beijing, China. pp.240-247, Oct. 2009.

VR training application for AR-assisted pick and place activities in logistics warehouses

Vasileiou Vasileios-Christos[1], Sidiropoulos Vasileios[1], Bechtsis Dimitrios[1] and Vlachos Dimitrios[2]

[1]Department of Industrial Engineering and Management, International Hellenic University, Sindos, 57400, Greece,
[2]Department of Mechanical Engineering, Aristotle University of Thessaloniki, 54124, Greece

Exploring the frontier of innovation in industrial workflows, our revolutionary application delves into the transformative potential of augmented reality (AR) within a virtual reality (VR) environment. This novel approach aims to optimize industrial operations by testing the impact of AR in a simulated VR environment, offering unique insights beyond real-world applications. Process optimization is pivotal in enhancing efficiency and overall productivity in industries [1]. As industries evolve, the incorporation of immersive technologies, such as augmented reality (AR) and virtual reality (VR) has emerged as a game-changer [2],[3]. In the context outlined, the authors envision the establishment of a logistics center where a revolutionary VR application, as discussed by Xie et al. [4], will be utilized for the training and guidance of employees. In the developed application the trainee must complete a picking process in a virtual warehouse with marked rows, columns, and floors. The proposed mission is to collect boxes from a specific order provided to the trainee while entering the virtual world. The trainee will be equipped with a tablet that displays the list of predefined boxes they need to pick. The order indicates a set of boxes located in specific rows, columns and floors in the warehouse. For example, the box could be found in row 1, place 26, with the corresponding code in the tablet being R1P26. For picking the boxes from these spots, we propose three distinct approaches namely (i) the first guidance level with full AR support where the platform sequentially guides the trainee to the boxes, (ii) the intermediate level where some AR features are provided for sequentially guiding the trainee to the boxes and (iii) the third level where the trainee can make decisions and navigate in the facility without any visual assistance at his own pace.

At the first level, an arrow is positioned prominently in front of the trainee, serving as a guide towards the actual boxes in the warehouse. Concurrently, a spotlight highlights the target box, offering an additional layer of visual assistance. This first level is designed to provide the utmost support to the employee, ensuring a seamless and efficient retrieval process. At the intermediate level, a smaller arrow serves as the primary guide, directing the trainee towards the facility layout for the picking process This provides a further degree of independence while allowing the employee to be engaged to the virtual facility. In the final level, the platform poses a unique challenge to the trainee by eliminating all the supportive AR technologies. This level intentionally excludes external support, emphasizing the need for self-reliance in the box-picking process. In this stage, the user relies solely on the picking list thus evaluating the trainee's ability to navigate the industrial facility and pick the boxes in any order. This scenario could be directly compared to the AR-enabled scenarios and provide insights into the impact of the AR assistance in the overall process. Throughout the training process, the platform records the overall time of the picking process and the box selection actions of the trainee, creating a valuable dataset for further analysis.

Figure 1. Logistics warehouse
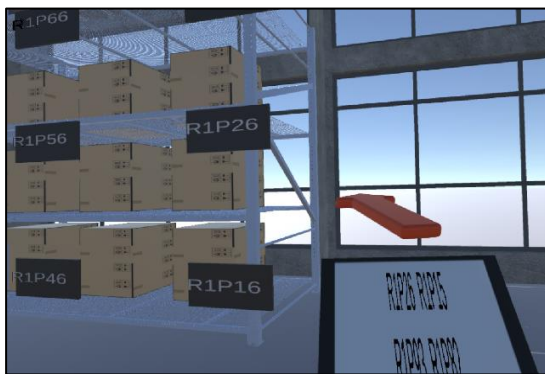

Figure 2. Full AR Support Level

Figure 3. Partial AR Support Level

Figure 4. No AR support Level

The scope of the developed application is to understand the impact of VR training tools on employees, whether AR technologies can be used to support the picking process and the degree of AR support needed for supporting daily picking activities. After testing the platform, the trainees were thrilled with the VR tool and accepted the use of the platform for training purposes. Even though the trainees were initially introduced to the full AR support scenario and gradually the level of assistance was reduced, the actual findings indicated that the number of mistakes and the time for completion was significantly less in the full AR support scenario. This indicates the significance of AR assistance in daily warehouse activities.

Expanding beyond training tasks, this application can integrate into operational scenarios. In logistics environments, the VR application can communicate with the warehouse database outlining product locations and recreate the products with their specific location in the VR environment. Afterwards, it can facilitate the implementation of different levels of augmented reality layers necessary to support employees in navigating for the completion of tasks assigned to them, displaying them through AR glasses. Through communication with the database, the application can autonomously record data and utilizes machine learning models for real-time routing optimization. Additionally, the implementation of preliminary testing in a virtual environment ensures the efficacy of optimized routes and AR layers before adapting them in the real world contributing with this way to enhanced overall operational efficiency.

References

[1] V. Tripathi, S. Chattopadhyaya, A.K. Mukhopadhyay, S. Sharma, C. Li, S. Singh, W. Saleem, B. Salah, and A. Mohamed, "Recent Progression Developments on Process Optimization Approach for Inherent Issues in Production Shop Floor Management for Industry 4.0," Processes, vol. 10, no. 8, p. 1587, Aug. 12, 2022. DOI: 10.3390/pr10081587.

[2] P. Begout, S. Kubicki, E. Bricard, and T. Duval, "Augmented Reality Authoring of Digital Twins: Design, Implementation and Evaluation in an Industry 4.0 Context," Front. Virtual Real., vol. 3, article 918685, June 30, 2022. DOI: 10.3389/frvir.2022.918685.

[3] A. C. Firu, A. I. Tapîrdea, A. I. Feier, and G. Drăghici, "Virtual reality in the automotive field in industry 4.0," Materials Today: Proceedings, vol. 45, no. 5, pp. 4177-4182, 2021. https://doi.org/10.1016/j.matpr.2020.12.037

[4] B. Xie, H. Liu, R. Alghofaili, Y. Zhang, Y. Jiang, F. D. Lobo, C. Li, W. Li, H. Huang, M. Akdere, C. Mousas, and L.-F. Yu, "A Review on Virtual Reality Skill Training Applications," Front. Virtual Real., vol. 2, article 645153, April 30, 2021. DOI: 10.3389/frvir.2021.645153.

Is Warm-Up Necessary for Function Generators? – Instrument Performance Verification Test

Vassios V.D., Hatzopoulos A.T., Tsiakmakis K., Papadopoulou M.S.

Department of Information and Electronic Engineering
International Hellenic University, Sindos, Thessaloniki, Greece

Abstract— **This work presents the performance changes of a function generator, during its warm-up time. An automated measurement and performance verification system is implemented for this generator, according to manufacturer's instructions. Due to the automated procedure, which is controlled by a computer application, the performance test is executed in only ten minutes. This system measures every ten minutes, during the warm-up period, the performance of the frequency generator. The measurements shows the change of the generator's behavior as the recommended time is completed. The improvement in the performance is obvious and shows that for better accuracy the warm-up should be extended.**

Index Terms — **Warm-up time, Performance verification, Automated calibration system, function generator warm-up.**

I. Introduction

THE measuring instruments are accompanied by the manufacturer's specification datasheet. According to these, accuracy and uncertainty of the measurements can be calculated. Accredited calibration laboratories that follow international operating standards, such as ISO17025, are obliged to use calibrated equipment. At short intervals they can verify their measuring accuracy with verification tests. At longer regular intervals, usually every year, the laboratories perform calibration of the equipment, according to approved procedures. These calibration procedures are costly due to required expensive equipment but greatly improve the accuracy and uncertainty of their measurements.

In simpler or educational laboratories, where high precision and certificates are not required, personnel take care of the good use and maintenance of measuring instruments and adopt the accuracy of measurements stated by the manufacturer. Since the characteristics of the instruments change over time, the manufacturers recommend that verification tests should be done regularly, to ensure reliability in the measurement accuracy.

Almost all measuring instruments state the necessary environmental operating conditions along with the characteristics of the measurements in their user's manual. In addition, a warm-up period is indicated on electrical measuring instruments to ensure that the instrument is ready to measure with the stated accuracy. In university laboratories there are instruments for students to perform the laboratory measurements but there is usually not enough time for warm-up. Some measuring instruments only need 15-30 minutes of warm-up but provide low accuracy. The instruments with better accuracy require up to 1 hour warm-up, while calibration and performance verification instruments require 1-2 days.

The purpose of this work is to monitor the change in the reliability of a measuring instrument in relation to the time it has been warmed up. The instrument chosen is a function generator (FG) that requires a 30-minute warm-up [1]. A performance verification measurement system, similar to those used in calibration procedures, is implemented to evaluate the generator's behavior [2]. Of course, no calibration of the generator or estimation of measurement uncertainty can be done. Simply, comparative measurements are made that show the change of the generator's characteristics over time.

II. Experimental Setup

For this study of performance versus warm-up time, a Siglent SDG1025 FG is used as device under test. The manufacturer's proposed warm-up time is 30 minutes. In order to make enough evaluations of the FG's performance, a very fast performance verification test system is implemented.

The first stage of this study is the development of the performance verification testing system. This automated measuring system is similar with the calibration systems, but without their accuracy, because of the uncontrolled environmental conditions and the uncertified measuring capabilities. The system consists of the following equipment.

i. FG Siglent SDG1025 (25MHz)
ii. Digital Multimeter (DMM) Fluke 8845A
iii. Oscilloscope Siglent SDS1102CML+
iv. Personal Computer (PC)
v. GPIB controller National Instruments GPIB-USB-B
vi. Software LabVIEW

The accuracy of the equipment is not important, because in this work, only the change of FG's main characteristics during the warm-up period is recorded and not the accuracy of them.

According to the FG's manufacturer's service manual, the following performance tests must be executed.

i. DC Output Verification
ii. Duty Cycle Verification for Square Pulse
iii. AC Amplitude Verification
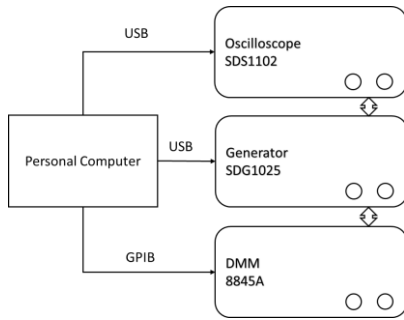iv. Frequency Response Verification

Fig. 1. Experimental setup of the automated measuring system

The first test is executed for FG's output channels connected to the DMM to measure different values of DC offset voltages.

The second test is executed with the oscilloscope for 3 different settings (20%, 50% and 80%) of duty cycle on a square pulse signal (4Vpp@100kHz), for both output channels.

The third test is executed with the oscilloscope instead of the proposed power meter and verifies the amplitude voltage settings of a sine signal at the frequency of 100kHz.

The fourth test is executed again with the oscilloscope instead of the proposed power meter and verifies the stable amplitude setting (1Vp) over the full frequency range.

On PC runs an application designed in the LabVIEW programming language. The aim of the use of PC and software application is to execute the performance tests in a very short period of ten minutes. This application is designed for optimal speed, without reducing the accuracy. This is achieved by implementing a low level programming, modifying properly the instrument's drivers to avoid all the unnecessary initializations and reconfigurations.
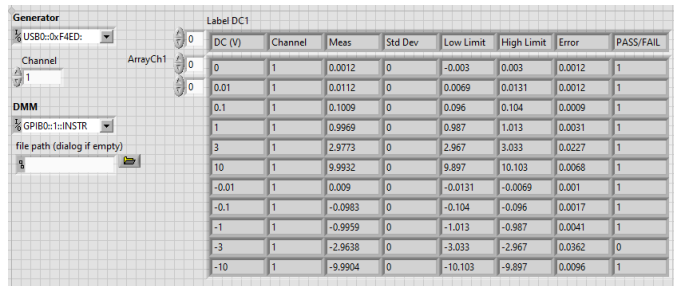

Fig. 2. The labview "virtual instrument" showing the DC Output test

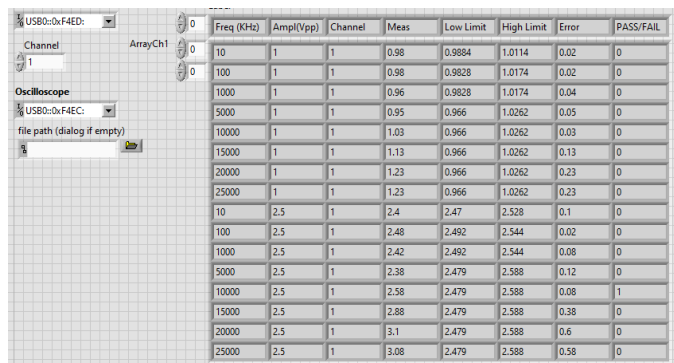The measurements are shown on the PC's screen and recorded on a file for later use.

Fig. 3. The labview "virtual instrument" showing the Frequency Response test

III. EVALUATION OF MEASUREMENTS

The second stage of this work is the evaluation of the measurements. The first set of measurements was taken immediately after powering on the FG (0 mins). The rest equipment was warmed-up properly (at least 1 hour). The next measurement sets were taken at 10 minutes, 20 minutes, 30 minutes and 240 minutes. The last set is showing the final and stable value of the measured parameters.

Table 1 is showing the measurements of the first performance verification test, which is the DC Offset Voltage Setting for Channel 1. Figure 4 is showing the percentage error of the DC Offset vs warm-up time. It is clear that the offset voltage has small error from the first minutes but is getting even smaller as time increases. The largest error is appearing for the smallest offset voltages, 100mVolts and -100mVolts. For FG's channel 2 the error is smaller. The other DC voltage settings, i.e. ±3Volts and ±10Volts have the same or smaller error and are not presented in table 1 and in figure 4.

TABLE 1. DC Offset Voltage Channel 1

DC Offset Ch1				
	0min	10min	20min	30min	240min
DC (V)	Meas (V)	Meas (V)	Meas (V)	Meas (V)	Meas (V)
0	0.0012	0.0005	0.0007	0.0004	0.0002
0.1	0.1009	0.1004	0.1006	0.1003	0.1002
10	9.9932	10.0073	10.0038	10.0092	10.0132
-0.1	-0.0983	-0.099	-0.0988	-0.0991	-0.0993
-10	-9.9904	-10.0142	-10.0082	-10.0176	-10.0252
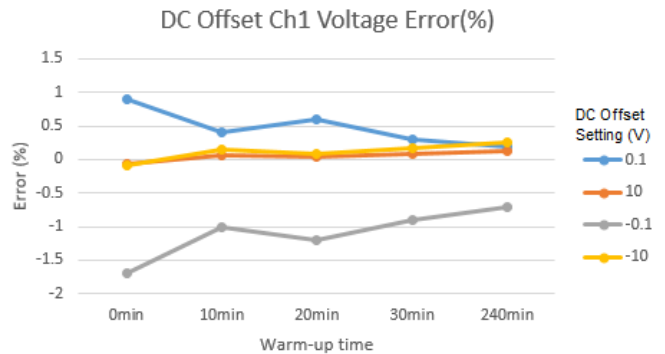
Fig. 4. DC Offset Ch1 voltage error showing improvement as time increases

Table 2 has the measurements for the Duty Cycle settings of 20%, 50% and 80% on a square signal of 4Vpp at 100kHz. Figure 5 shows the percentage error versus time. For duty cycle of 20% there is a great improvement after time but the other two settings have small error from the beginning. Same corrections appear also for the channel 2. This behavior is probably because of the oscilloscope's not stable image and reduced resolution.

TABLE 2. Duty Cycle Channel 1 (%)

Duty Cycle (%) Ch1				
	0min	10min	20min	30min	240min
DC (%)	Meas (%)	Meas (%)	Meas (%)	Meas (%)	Meas (%)
20	19.4	19.4	19.9	19.9	19.9
50	50.05	50	50	50.6	50.5
80	79.5	80	79.5	80	80.1

Fig. 5. Duty Cycle Ch1 Error (%)

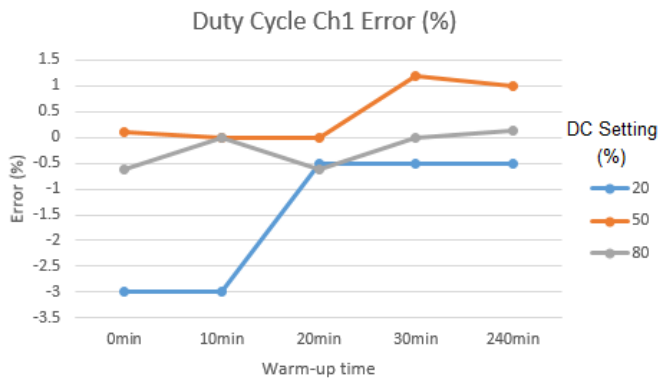For the third performance test, the AC amplitude setting at the frequency of 100kHz is interesting. The graph for 40mVpp has an increment after 240 minutes which can be explained by a random error, like the cable unstable connection. All the other measurements show a stable performance over the warm-up time.

TABLE 3. AC Amplitude Channel 1

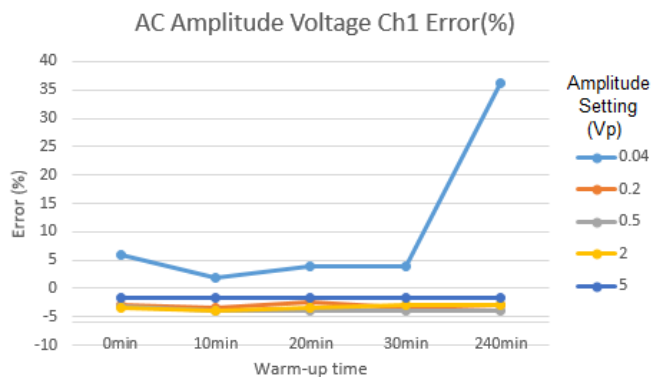| AC Amplitude Verification Ch1					
	0min	10min	20min	30min	240min
Ampl(Vpp)	Meas	Meas	Meas	Meas	Meas
0.04	0.0424	0.0408	0.0416	0.0416	0.0545
0.2	0.194	0.193	0.195	0.193	0.194
0.5	0.484	0.48	0.48	0.48	0.48
2	1.93	1.92	1.93	1.94	1.94
5	4.92	4.92	4.92	4.92	4.92

Fig. 6. AC Amplitude Channel 1

The last performance verification test is the AC frequency response. For both channels a sine signal with amplitude 1Vp at 25MHz is applied. Instead of the table with measurements, it is better to present the two figures that show the measurements separated in two groups.

The measurements with the smaller error are these at lower frequencies. At higher frequencies, the error is very large due to the replacement of the suggested power meter instrument by an oscilloscope. Both channels at the frequency of 25MHz show improvement with time.
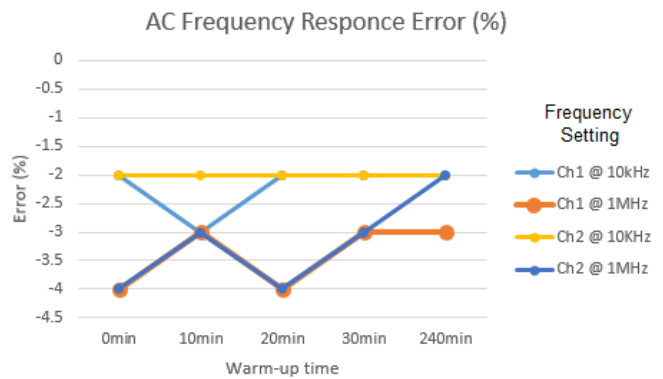

Fig. 7. AC Frequency Response for both channels at low frequencies
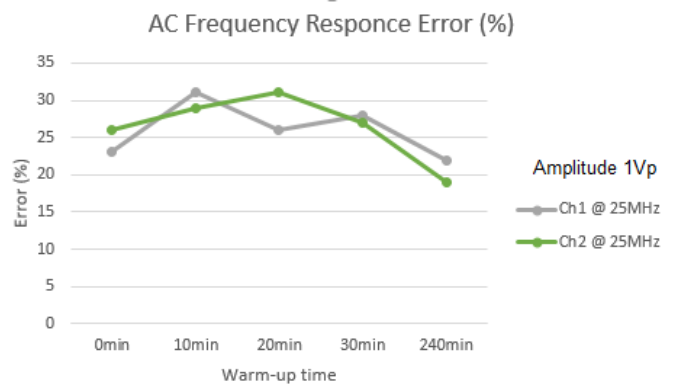
Fig. 8. AC Frequency Response for both channels at high frequencies

IV. EXCESSIVELY FREQUENT MEASUREMENTS OVER TIME

All the tests show that while the generator warms-up, the measured characteristics come closer to the nominal values, as expected. In the third stage of this work, a more detailed investigation is taking place. During a period of 120 minutes, with a sampling rate of only 10 seconds, the system is measuring continuously each characteristic separately, avoiding cable disconnections and rearrangements.

In order to achieve this goal, a new version of the measuring application is made exclusively for each generator's parameter. Figure 9 shows the application for measuring continuously the DC offset voltage on output channel 1.

Fig. 9. Application for very fast DC offset voltage measurements

A DC offset 1Volt is configured on channel 1 on a "cold" FG and is measured as soon as the instrument is powered on. It is obvious that for the first few minutes, the error is significant but is reduced very fast. The measurements are shown in figure 10. Channel 2 shows the same evolution like channel 1 output.

Fig. 10. Detailed DC offset 1 Volt setting evolution

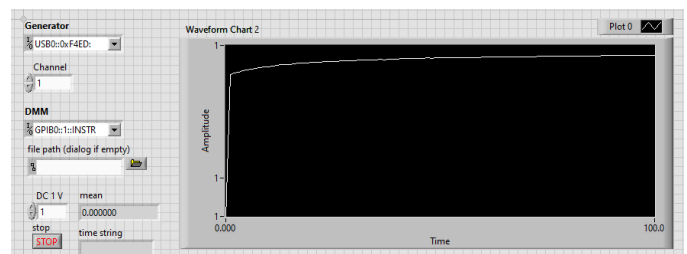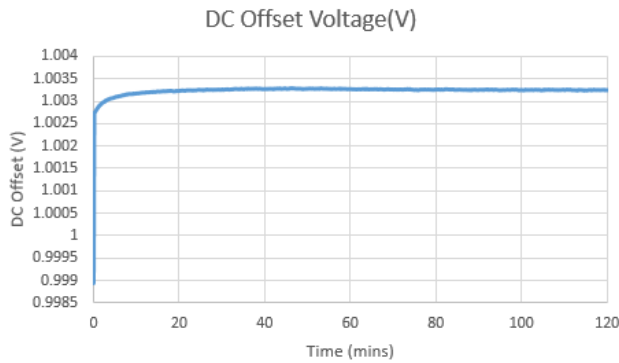Figure 11 shows the sine amplitude evolution during warm-up time, with the same high sampling rate (10 secondss). A sine signal of 1Vp at 1kHz is set on the FG and is measured with the DMM, which has a significant better accuracy and resolution that the oscilloscope that was used for the third performance verification test [3-4]. It is clearly shown that the FG continues to improve the AC amplitude characteristic significantly after the suggested 30 minutes warm-up time.
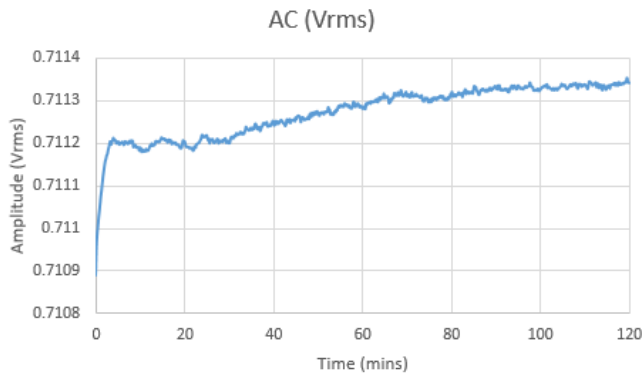

Fig. 11. Detailed AC amplitude 1 Vp setting evolution (measured in Vrms by DMM)

The frequency setting of the FG evolution is not shown because is quite satisfying from the first minutes and has very small variations.

V. CONCLUSION

This work has two parts, the implementation of a very fast performance verification test for a function generator and the investigation of the needed warm-up time. The first part is necessary for the execution of as many measurements sets as possible during the first minutes.

The second part showed that for this generator, the manufacturer proposes 30 minutes warm-up period but some parameters have been stabilized very soon while other need more time. Furthermore, DC offset and Duty Cycle seems to improve even more as time increases.

Even more detailed measurements every 10 seconds shows that for the first 5 minutes, some FG's characteristics have a significant error which is quickly reduced. But, the amplitude

setting for the first 30 minutes of warm-up must be considered as unstable.

So, for measurements with reduced accuracy, the warm-up time can be up to 60 minutes. For further warm-up time, the measurements show that the accuracy improvement has a lower rate.

For future, it would be interesting to use calibrated DMM and frequency counter and investigate the needed warm-up time to the meet the nominal accuracy specifications.

REFERENCES

[1] SIGLENT TECHNOLOGIES CO., LTD, "SDG1000 Series Function/Arbitrary Waveform Generator, Service Manual", 2014
[2] SIGLENT TECHNOLOGIES CO., LTD, "SDG1000 Series Function/Arbitrary Waveform Generator, User Manual", 2014
[3] FLUKE CORPORATION, "FLUKE 8845A/8846A User's Manual", 3/2011
[4] SIGLENT TECHNOLOGIES CO., LTD, "SDS1000CML Series Digital Oscilloscope, Datasheet", 2013

Theoretical Model of Acoustic Power Transfer Through Solids

Ippokratis Kochliaridis and Michail E. Kiziroglou,

Department of Industrial Engineering and Management, International Hellenic University, Greece
Email: m.kiziroglou@gmail.com , Ippokratis_polichni@hotmail.com

Abstract—**Acoustic Power Transfer is a relatively new technology. It i's a modern type of a wireless interface, where data signals and supply voltages are transmitted, with the use of Mechanical Waves, through a medium [1][2]. The simplest application of such systems is the measurement of frequency response for audio speakers. It consists of a variable Signal Generator, a Measuring Amplifier which drives an acoustic source and the Loudspeaker Driver. The receiver contains a Microphone Circuit with a Level Recorder [3]. Acoustic Power Transfer could have many applications, such as: Cochlear Implants, Sonar Systems and Wireless Charging. However, it's a new technology, so it needs further investigation.**

I. INTRODUCTION

There are many wireless interfaces, such as: RFID. However, these technologies in some cases, could be problematic. For example, electromagnetic signals couldn't penetrate metallic surfaces, due to Faraday Shielding Effect, or are limited to a very low Bandwidth (<100 Hz) [4][5]. In addition, there are many marine sensor applications, which require penetration thought solid metal walls. In such cases, drilling is not preferable as a solution for signal or power coupling through metallic walls, due to reliability and sealing problems. As a result, data and power supply transmission using acoustic waves, from an acoustic source to a receiver, could be a promising solution [2].

II. SYSTEM ARRANGEMENT

The figure 1 represents the Block Diagram, of a simplified Acoustic Power Transfer System. The Transmitter (TX) consists of a signal generator, a power amplifier and an acoustic source, which is a Piezoelectric Ultrasound Driver [1]. The Receiver consist of a Piezoelectric Microphone and a network circuit, which charges a battery. The transmitter uses the piezoelectric effect to generate acoustic waves from electrical power [1]. The receiver converts acoustic waves into electrical power, again using the piezoelectric effect. The medium, could be air, metals and even tissue in the case of medical implants.

A. An application system

Figure 2 shows a typical arrangement of an Acoustic Power

Transfer System. It consist of a medium of transfer , which is a metallic surface, an acoustic source, which is a piezoelectric ultrasound driver and the receiver in the other side which is a piezoelectric transducer also. The gap between the metallic wall and the diaphragms is filled with some type of glue suitable for acoustic interfacing. This arrangement is often referred to as the -One Dimension Propagative Model (ODPM) [2].

B. Characteristics of the System

A study has shown that this type of arrangement could transmit power over 100 W, for 10 min and with 60% efficiency, though a 57.2 mm steel surface [6]. Lawry et al [7] have proposed a method to calculate load impedance, for the receiver output, in order to achieve higher efficiency.

Beyond Wireless Power Transfer, this arrangement can also be used for acoustic data transfer. However the Data Rate is relatively small, in the range of 55 kbps [8]. In order to achieve higher data rates, signal processing technics, such as Orthogonal Frequency Division Multiplexing (OFDM) [2] should to be used. In a case of an Array, with seven Piezoelectric Drivers and Microphones, in the Transmitter and the Receiver respectively, a maximum Data Rate of up to 700 Mbps was demonstrated [9].
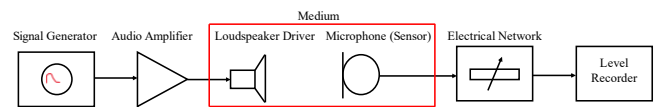

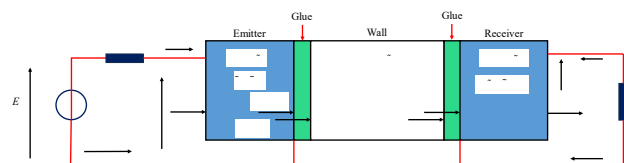Fig. 1. A simplified block diagram, which illustrates the transmitter and the receiver.

Fig. 2. An arrangement of an Acoustic Power of Transfer System according to Freychet et al [2].

C. Modeling the System – Equivalent Circuits

The technical characteristics of a Piezoelectric Driver or a Receiver, could be expressed as an equivalent electrical circuit network. The most common mathematical models are the Mason model and the Krimholtz, Leedom, and Matthaei (KLM) [10]. The Mason concept was to present Electrical, Mechanical and Acoustical properties of a transducer, as an electrical line. The Figure 3 represents the mason equivalent electrical system.
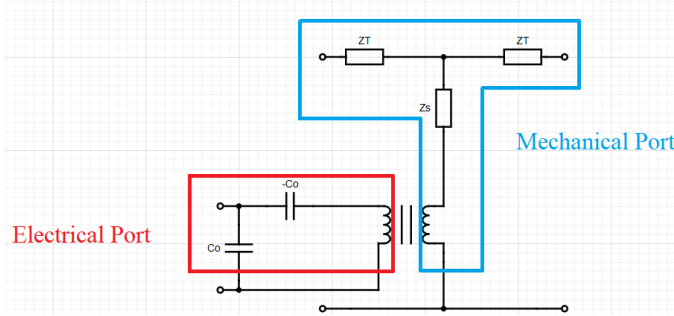

Fig. 3 The equivalent electrical network of the mason model.

Figure 3 illustrates that a piezoelectric transducer, consists of a mechanical part (the network with 3 blue Impedances) and an electrical stage (the positive and negative capacity). The KLM model is simpler, because it eliminates the negative capacity [10]. The figure 4 illustrates the mathematical concept of Mason, applied in a complete electro-acoustical signal transfer system:

The first stage (Green), illustrates the equivalent electrical circuit of the Acoustic Source. The stage with the 3 blue Impedances, represents the Matching Layer. This corresponds to the gap between the diaphragm of the driver and the metallic surface. The Orange stage represents the impedance of the metallic medium. Finally, the red impedances is the receiver circuit.

The complete set of equations which describe the Acoustic Power Transfer System, given in figure 2, could be summarized into a single matrix given in equation (1) [2]:

$$
\begin{bmatrix} F_1 \\ -F_2 \\ U_1 \\ F_2 \\ -F_3 \\ F_3 \\ -F_4 \\ F_4 \\ -F_5 \\ F_5 \\ -F_6 \\ U_2 \end{bmatrix} =
\begin{bmatrix}
X_{11}^1 & X_{12}^1 & X_{13}^1 & 0 & 0 & 0 & 0 & 0 \\
X_{12}^1 & X_{11}^1 & -X_{13}^1 & 0 & 0 & 0 & 0 & 0 \\
X_{13}^1 & -X_{13}^1 & X_{33}^1 & 0 & 0 & 0 & 0 & 0 \\
0 & X_{11}^2 & 0 & X_{12}^2 & 0 & 0 & 0 & 0 \\
0 & X_{12}^2 & 0 & X_{11}^2 & 0 & 0 & 0 & 0 \\
0 & 0 & 0 & X_{11}^3 & X_{12}^3 & 0 & 0 & 0 \\
0 & 0 & 0 & X_{12}^3 & X_{11}^3 & 0 & 0 & 0 \\
0 & 0 & 0 & 0 & X_{11}^4 & X_{12}^4 & 0 & 0 \\
0 & 0 & 0 & 0 & X_{12}^4 & X_{11}^4 & 0 & 0 \\
0 & 0 & 0 & 0 & 0 & X_{11}^5 & X_{12}^5 & X_{13}^5 \\
0 & 0 & 0 & 0 & 0 & X_{12}^5 & X_{11}^5 & -X_{13}^5 \\
0 & 0 & 0 & 0 & 0 & X_{13}^5 & -X_{13}^5 & X_{33}^5
\end{bmatrix}
\begin{bmatrix} V_1 \\ V_2 \\ I_1 \\ V_3 \\ V_4 \\ V_5 \\ V_6 \\ I_2 \end{bmatrix}
$$

(5)

In this matrix for a five layer arrangement, Vn corresponds to the speed at the nth interface, and Fn corresponds to the force at the nth interface acting on the material at the right of the interface [2]. U_n are the voltages, which apply across two consecutive layers of the transducers, I_n are the currents and finally X_n are related to the Acoustic Characteristic Impendance of each layer. An example which demonstrates the practical use of this Transfer-Function Matrix, can be found in the determination of Input Force F_1 (It's the force which applies, in the first side of the Transducer-Driver) as follows:

$$F_1 = X_{11}^1 * V_1 \; + \; X_{12}^1 * V_2 \; + \; X_{13}^1 * I_1 \; + \; 0 * V_3 \; + \; 0 * V_4 \; + \; 0 * V_5 \; + \; ......0 * I_2 \; (1).$$

where: V_1 is the velocity which applies in the first side of the Transducer-Driver, X is the Acoustic Impedance of the transducer in the first side, V_2 is the velocity which applies in the second side of the Transducer, X_{12}^1 is accordingly the Acoustic Impendence in the second side of the Transducer, X is the Acoustic Impendence of whole Transmitter and I_1 is the supply current of the Acoustic Source.

The 1st matrix's element (Acoustic Impendence X_{11}^1), according to Freychet [2], is a result from the mathematical relationship 2:

$$X_{11}^n = \frac{\tilde{z}_n^m}{\tan{(\tilde{k}_n x_n)}} \quad (2).$$

Where: x_n is the surface (layer) thickness. $\tilde{k}_n$ is the wave number [2] given by equation 3:

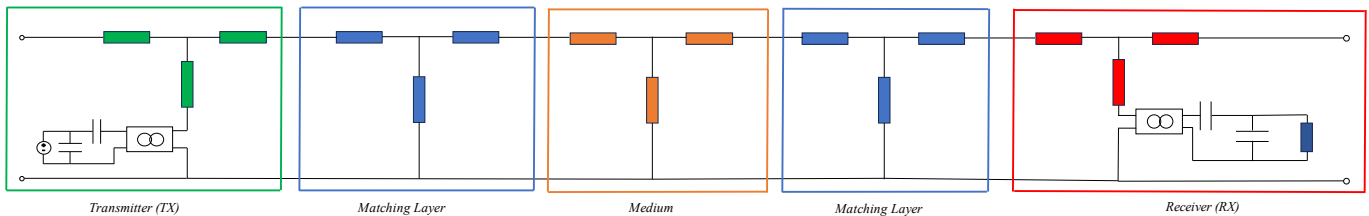$$\tilde{k}_n = \frac{\omega}{\tilde{c}_n} \; (3),$$

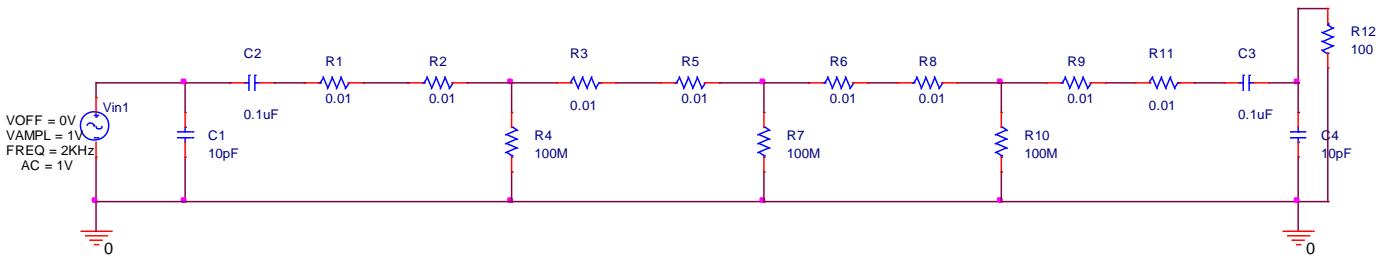Fig. 4. The equivalent electrical network in the whole System.

Fig. 6 A simplified electrical network of Mason's equivalent circuit, for future investigation.

Here, ω is the signal angular frequency. Finally, $\tilde{Z}_n^m$, is the Mechanical Characteristic Impendence of the layer [2], which is defined by equation 4:

$$\tilde{Z}_n^m = S\tilde{Z}_n^a = S\rho_n\tilde{c}_n \ (4).$$

In this equation ρ_n is the density, S the surface of the layer and $\tilde{c}_n$ the longitudinal speed of sound.

III. CONCLUSION

In this paper a theoretical analysis of acoustic power transfer through solids was presented. The analysis is based on the standard models of Freychet and Mason. A corresponding simulation model was designed using the Cadence circuit design software, as indicatively shown in Figure 6. Subsequent steps of this work involves calculation of acoustic power transfer through metal plates and experimental work to investigate the possibility of using acoustic lenses and reflectors in order to maximize power deliver to specific locations.

REFERENCES

[1] Sung Q Lee, Woosub Youm and Gunn Hwang, '' Biocompatible wireless power transferring based on ultrasonic resonance devices'', *2013 Acoustical Society of America, Received 22 Jan 2013; published 2 Jun 2013.*

[2] Freychet *et al* 2020 *Eng,* ''Analytical optimization of piezoelectric acoustic power transfer systems'', *Eng. Res. Express 2 (2020) 045022.*

[3] Παπανικολάου Γ. Ηλεκτροακουστικές μετρήσεις, *University Studio Press σελίδα: 60.*

[4] Imoru O, Jassal A, Polinder H, Nieuwkoop E, Tsado J and JimohA A 2013''An inductive power transfer thought metal object'', *1st Int. Future Energy Electronics Conf. (IFEEC) 2013 1st Int. Future Energy Electronics Conf. (IFEEC) 246 – 51.*

[5] Garraud N, Alessandri B, Gasnier P, ArnoldD and Boisseau S 2019, ''Optimization of a magnetodynamic receiver for versatile low-frequency wireless power transfer'' 19th Int. Conf. on Micro and Nanotechnology for Power Generation and Energy Conversion Applications (PowerMEMS) 2019 1-6.

[6] Wilt K R, Scarton H A, Saulnier GJ, Lawry TJ and Ashdown JD ''2013 High-power operation of acoustic-electric power feedthroughs through thick metallic barriers'' *ASME 2012 Int. Mechanical Engineering Congress and Exposition (American Society of Mechanical Engineers Digital Collection) 475 – 82.*

[7] Lawry T J, Wilt K R, Roa-Prada S, Ashdown J D, Saulnier G J, Scarton H A, Das P K and Pinezich J D, '' 2010 Electrical optimization of power delivery through thick steel barriers using piezoelectric transducers'' *Energy Harvesting and Storage: Materials, Devices and Applications 7683 768314.*

[8] Shoudy D A, Saulnier G J, Scarton H A, Das P K, Roa-Prada S, Ashdown J D and Gavens A J,''2007 An ultrasonic through-wall communication system with power harvesting'', *Proc. – IEEE Ultrasonics Symp. 1848-53.*

[9] Ashdown J D, Liu L, Saulnier G J and Wilt K R, ''2018 High-rate ultrasonic through-wall communications using MIMO-OFDM'' *IEEE Trans. Commun. 66 3381-93.*

[10] Hammid Basaeri, David B. Christensen, and Shad Roundy,'' A Review of Acoustic Power Transfer Bio-Medical Implants'' *Department of Mechanical Engineering, University of Utah, Salt Lake City, Utah, USA.*

Development of a Customized Prototyping board for the PN7160 Near Field Communication Microchip

A. Chatzimpaloglou and M. E. Kiziroglou
International Hellenic University, Greece

ABSTRACT—**In this work, a customized printed circuit board is presented for near field communication (NFC) research and prototyping. The board works at either 3.3 V or 3.7 V, which makes it suitable for powering from other embedded systems or from a battery. It has two interfaces Inter-Integrated Circuit (I2C) and Serial Peripheral Interface (SPI). The antenna has a width of $40mm^2$, a length of $40mm^2$ and tuned at 13.56MHz. The board design and fabrication are presented. Experimental tests for functionality and performance evaluation are underway.**

Index Terms— **Antenna, Bluetooth, I2C, Near Field Communication, Power Management, SPI.**

I. INTRODUCTION

NEAR Field Communication (NFC), Bluetooth, Wi-fi are all three wireless data transfer technologies. A disadvantage of the technology is the distance range. NFC is limited to a distance of 4 cm while Bluetooth can reach over 9 m and wi-fi over 45 m. Wi-Fi network is more costly and cannot send the huge data compared to wired technology. After all, Wi-Fi harms human health as it produces some radiation. Bluetooth cannot transfer the data of more than two devices, and data theft may occur due to the long data transfer distance.

Three advantages of NFC over the other two are that it consumes less power, which helps in faster data transfer, there is no interference in data transfers due to the short distance, and it is easy to use and set up.

The goal is the final realization of a microsystem actuation system with the exchange of information and energy via NFC, using mobile phones.

A comparison of features between the proposed system and the industrial evaluation board of the PN7161 chip is discussed in the next section. Subsequently, the board design is presented and discussed. Conclusions are summarized in the last section of the paper.

II. EVALUATION BOARDPROPOSED BOARD

The company NXP (Next eXPerience), manufacturer of the chip, has made two boards, one for the I2C interface and the other for SPI. In comparison with these commercially available evaluation boards, the proposed system introduces the following features:

1. It offers the possibility of providing both interfaces with the use of an appropriate switch.
2. It also implements the WKUP_REQ pin (Wake-up request pin) which is responsible for waking up the chip when it enters standby mode.
3. The power supply of the circuit is also different, according to the datasheet, configuration 1 (CFG1) is used to connect VBat

(Voltage Battery) to VDD(up) (Voltage Divider) in a battery like battery phone, while NXP uses configuration 2 (CFG2) to connect VDD(up) to an external power supply. This is illustrated in Fig. 1 and Fig. 2.
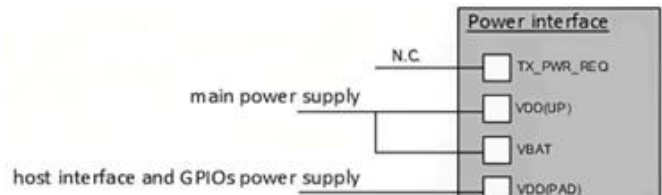

Fig. 1: CFG1 the battery voltage is directly used to generate the RF field).
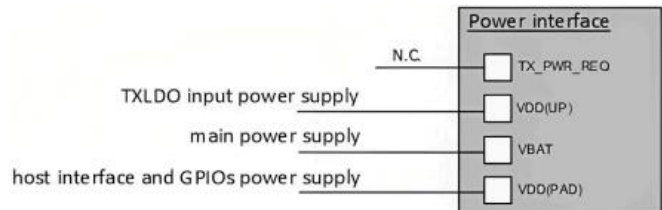
Fig. 2: CFG2 an extra external voltage is used to generate the RF field.

III. CIRCUIT DESIGN

The pinout of the PN7160 microchip is presented in Fig. 5.

The circuit design in eagle software. Pins 1,3,5,7 correspond to the I2C and SPI interfaces. The ability for selection between these two interfaces is implemented in the board by employing an 8-pin switch. By turning on 2, 3, 5, 7 and off 1,4,6,8 the I2C interface is selected. By turning off 2,3,5,7 and on 1,4,6,8 the SPI interface is selected.

The I2C interface needs pull-up resistors at pins 5 Serial Data (SDA) and 7 Serial Clock (SCL) to ensure that they remain at a high level when no device is driving them.

The PN7160 needs 3 external power supplies to operate, namely VBat, VDD(up) and VDD(pad). VBat from 2.8V to 5.5V is the main power supply of the controller. VDD(up) from 2.8V to 5.8V is the supply allowing to generate Transmitter LDO (TXLDO) with VDDtx output VDD(up) - 0.3V. Thus, VBat and VDD(up) are connected to an external battery 3.7V Fig. 1. VDD(pad) 3.3V, pin 6, is the power supply for the host interface and the General Purpose Input Outputs (GPIOs) are connected to an external power supply. So, the pins it should be connected are 12 VBAT2=13 VDD(UP)=28 VBAT/ 14 VDD(TX)=18 TVDD_IN =22 TVDD_IN2 / 26 VDD(A)= 27 VDD=31 VDD(D) which is internally connected to the output of the Dual Supply LDO (DSLDO). This is illustrated in Fig. 3.

Fig, 3: Power management diagram. DSLDO input VBat output VDD. TXLDO input VDD(up) output VDD(TX).

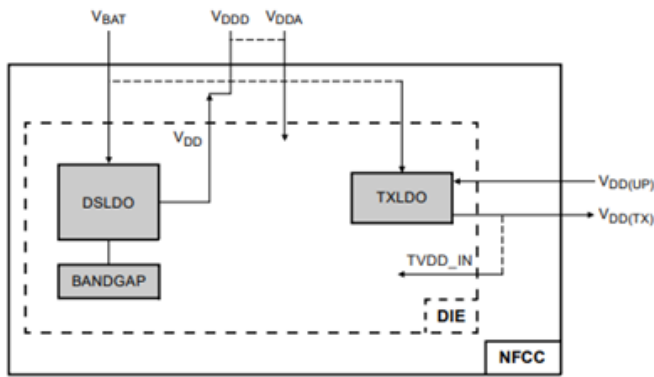Shunt capacitors are included on each voltage line following the manufacturer's instructions. These capacitors protect the lines from noise as well as transmission of the noise around lines and circuits.

In Fig. 6 the crystal circuit used for stabilizing the clock frequency is shown. The input and the output of the crystal are connected to pins 30 and 39 respectively It is important to connect a capacitor to both the input and the output that end up to ground. These capacitors help stabilize the oscillation frequency. They are placed in parallel with the crystal to help provide the necessary load capacitance for the crystal to oscillate at its desired frequency. Additionally, capacitors can help filter out any unwanted noise or signals that may be present in the circuit.

Light emitting diodes (LEDs) are included as indicators of correct input voltage levels.

Pins 2 Download request pin (DWL_REQ) download firmware,8 Interrupt Request (IRQ) confirmation of asynchronous data,10 V ENable pin (VEN) reset firmware and 39 (WKUP_REQ) are Host GPIOs pins and are connected to a connector.

Pins 32 to 36, 11 and 38 are unconnected by the manufacturer, they have no function.

Pins 23 Antenna 1 (ANT1) and 24 (ANT2) are optional. If connected, each pin needs a 12pF capacitor. These two pins act as a very low power Radiofrequency (RF) field detector. The NFC controller can detect the presence of an external magnetic field and notify the host system of its presence when the Near field communication controller (NFCC) is in the off state. Selecting it reduces the read range due to the additional loading of the antenna and thus it is not used by the proposed board and left it unconnected.

Pin 25 (VDD(HF)), is a power supply related to pins 23 and 24 and it is therefore also unconnected.

Pin 37 (DCDC_EN), is used as an alternative in the HVQFN version of the chip. The QFN version doesn't have the transmitter power request (TX_PWR_REQ) pin, which is available in the VFBG chip version as the main external power supply. In CFG2 a DC-DC converter is used.

Pin 40 (CLK_REQ), optimizes power consumption. This mechanism only applies when an external clock is used and not a crystal. In the proposed design it remains disconnected, as a crystal clock source is used.

Pins 4, 9, 20, 41 are connected to ground.

Figure 7 shows the antenna circuit connected to pins 15 Negative receiver input (RXN), 16 Positive receiver input (RXP), 19 Transmitter (TX2), 21 (TX1). The antenna circuit is divided into three parts, namely an Electromagnetic compatibility (EMC) filter a matching layer and the antenna itself.

The EMC filter is a low-pass filter used to attenuate either input high-frequency noise coming from the power cables or output noise from the system, to avoid polluting the antenna network.

The matching circuit implements impedance matching techniques for antennas aimed at maximum power transfer to the antenna. This allows a stronger antenna radiation and efficiency.

NFC antenna is represented as an inductor with Inductance (LANT) depends on the number of turns, Capacitance (CANT) out of the range of 1 pF - 30 pF the antenna may not be tunable for 13.56 MHz the antenna may not be tunable for 13.56 MHz, Resistance (RANT) depends on the track length, track width and copper thickness, Quality factor (Q) declares the number of losses inside the inductor and should be higher than 20 and Self-resonance frequency (fres) should be higher than 25 MHz parameters and can be comfortably tuned.

IV. BOARD

The final board has a width of 92 mm and a length of 50 mm. The antenna tunned at 32.56 MHz It consists of two layers, top Fig.4 and bottom Fig. 5. Both layers are grounded. In the top layer all the components are located and connected directly, the bottom layer helps to connect components that are in more distant positions.

The assembly steps of the board that were followed are:
1. Passing paste and visual inspection for the placement of the paste at all points.
2. Placement of the SMD components.
3. Baking in the oven, visual inspection under the microscope for the bonding of the components.
4. Finally power up the circuit and check the voltage levels, since everything is fine the experimental control with a target is the last step.

Fig. 4: Top layer assembled board.
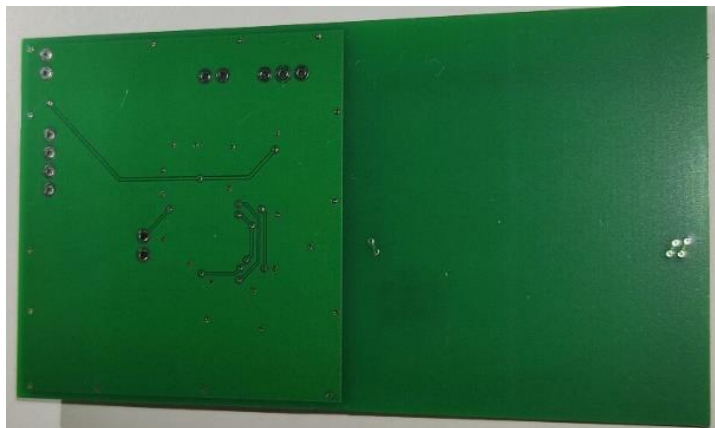
Fig. 5: Bottom layer assembled board.
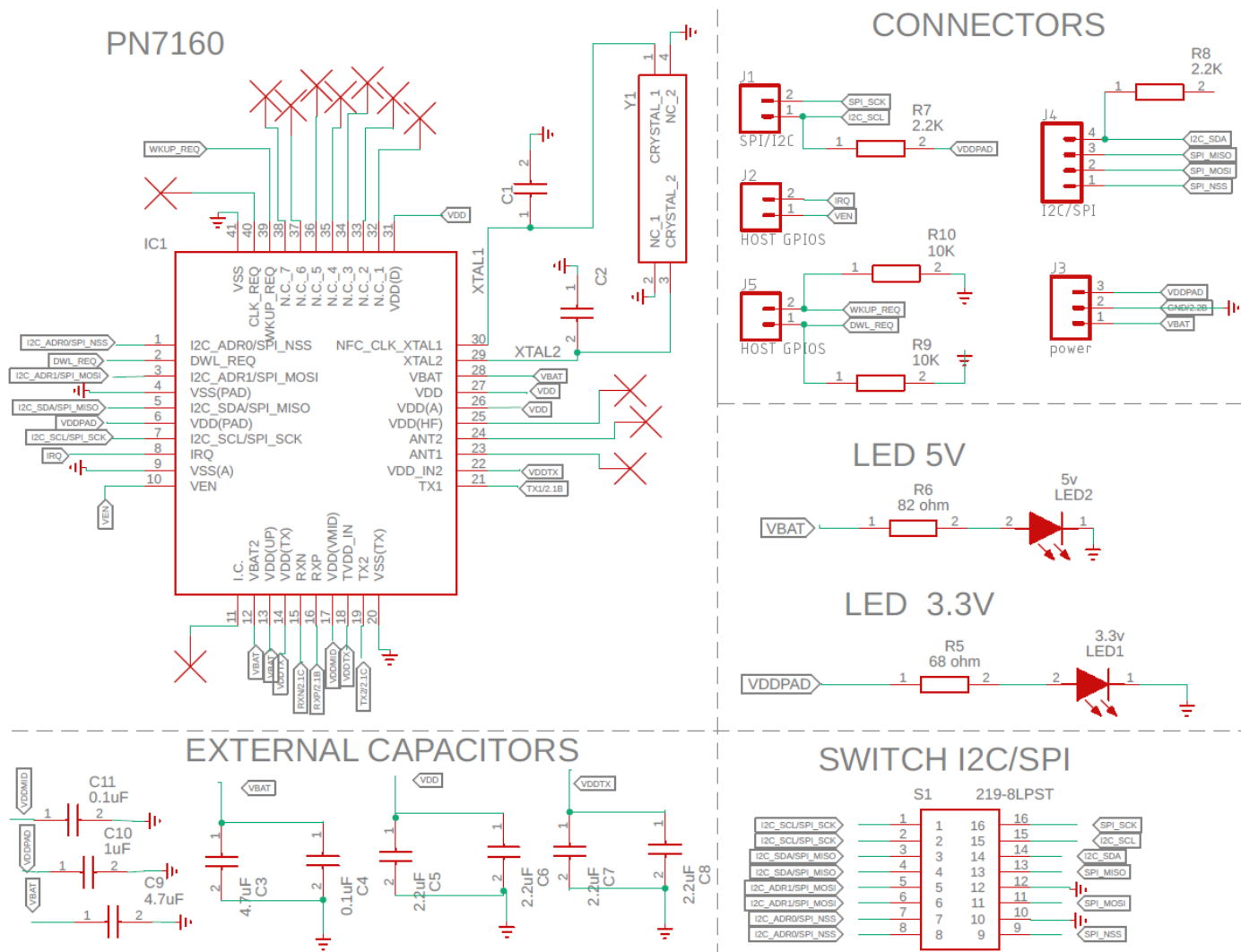
Fig. 6: Pinout PN7160, connections to connectors, leds indicators, external capacitors decupling and switch for I2C and SPI are presented.
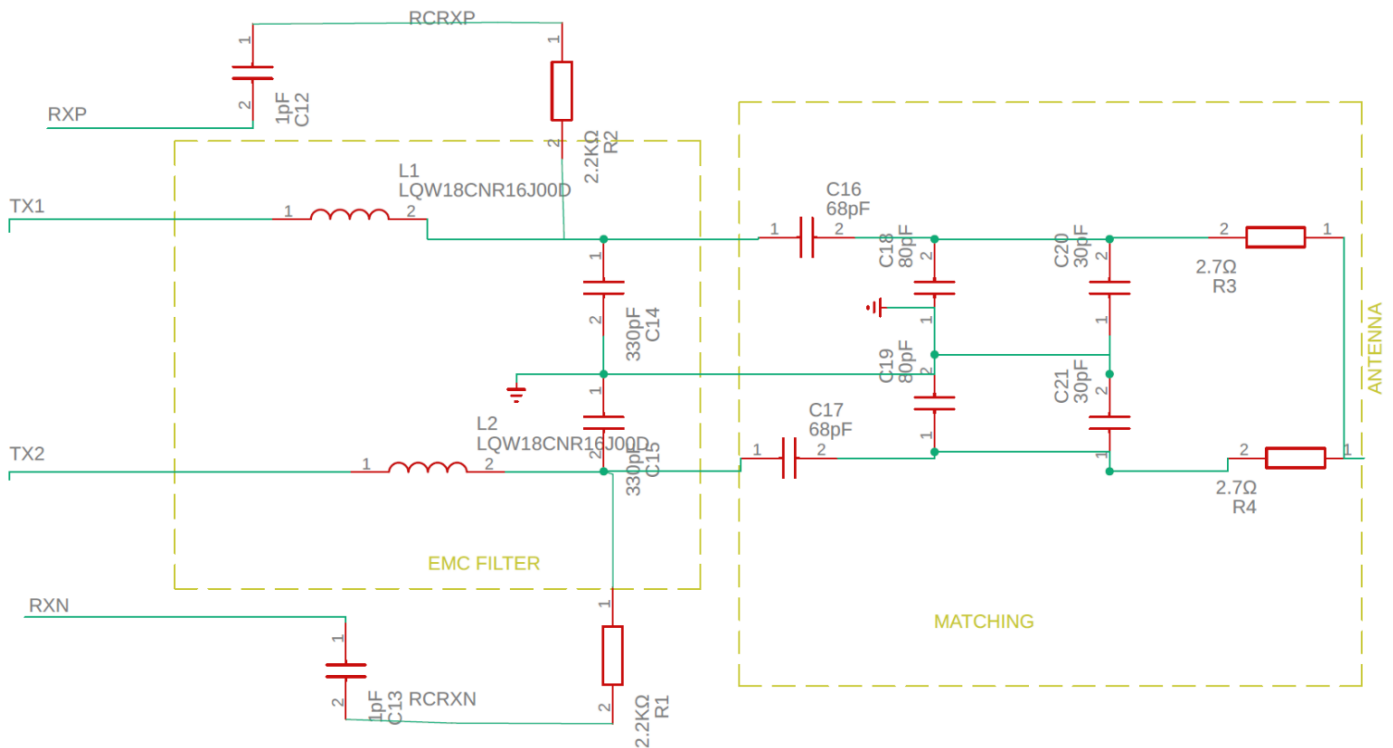
Fig. 7: Antenna circuit design.

V. CONCLUSION

Summarizing, in this paper compared to others and it turns out that it is faster, more economical and requires less
energy to operate. The board is suitable to be used by mobile phone providing two host interfaces I2C and SPI. Finally, the circuit design is analyzed and described with precision by illustrating the designs.

REFERENCES

[1]. PN7160_PN7161 Near Field Communication (NFC) controller Rev. 3.9 — 8 March 2023

[2]. UM10204 I 2C-bus specification and user manual Rev. 7.0 — 1 October 2021

[3]. AN13219 PN7160 antenna design and matching guide Rev. 1.4 — 9 November 2022

[4]. UM11496 PN7160 evaluation board Rev. 1.3 — 24 November 2022 AN12988 PN7160 hardware design guide Rev. 1.5 — 13 January 2023

[5]. SPI Block User Guide V02.07- 11 Dec 2002 by Motorola, Inc.

[6]. UM11232 NFC Antenna Design Tool User Guide Rev. 1.0 — 3 June 2019 User manual

Triboelectric energy harvesting for autonomous electronic devices

C. Tsamis[1], A. Bardakas[1], A. Segkos[1], G. Vekinis[1], C. A. Krontiras[2], S. Kennou[3]

[1]Institute of Nanoscience and Nanotechnology (INN), National Centre for Scientific Research "Demokritos",
Patr. Gregoriou E & 27 Neapoleos Str., Aghia Paraskevi, 15310 Athens, Greece
[2]Department of Physics, University of Patras, Rio University Campus, Patras GR-265 04, Greece
[3]Department of Chemical Engineering, University of Patras, 26504 Patras, Greece
e-mail:c.tsamis@inn.demokritos.gr

Abstract:

The triboelectric phenomenon has been identified as an attractive mechanism for the conversion of mechanical energy to electrical energy, since the first reported work by Fan et [1]. Triboelectric generators (TENGs) have been developed with an energy efficiency of up to 80% and output power up to 1KW/m^2. Triboelectricity is based on contact electrification and electrostatic induction between two surfaces that are in relative motion. It is thus expected that the triboelectric signal will depend on material properties as well as the surface roughness of the two surfaces. Several techniques have been proposed for controlling the surface roughness and thus tribogenerator performance.

In this review we will present technologies to engineer surface properties and roughness using various methodologies including deposition of nanoparticles, plasma etching, and nano-imprint and we will evaluate their influence on the performance of triboelectric generators. Examples of powering electronic devices in the maritime sector will be presented.
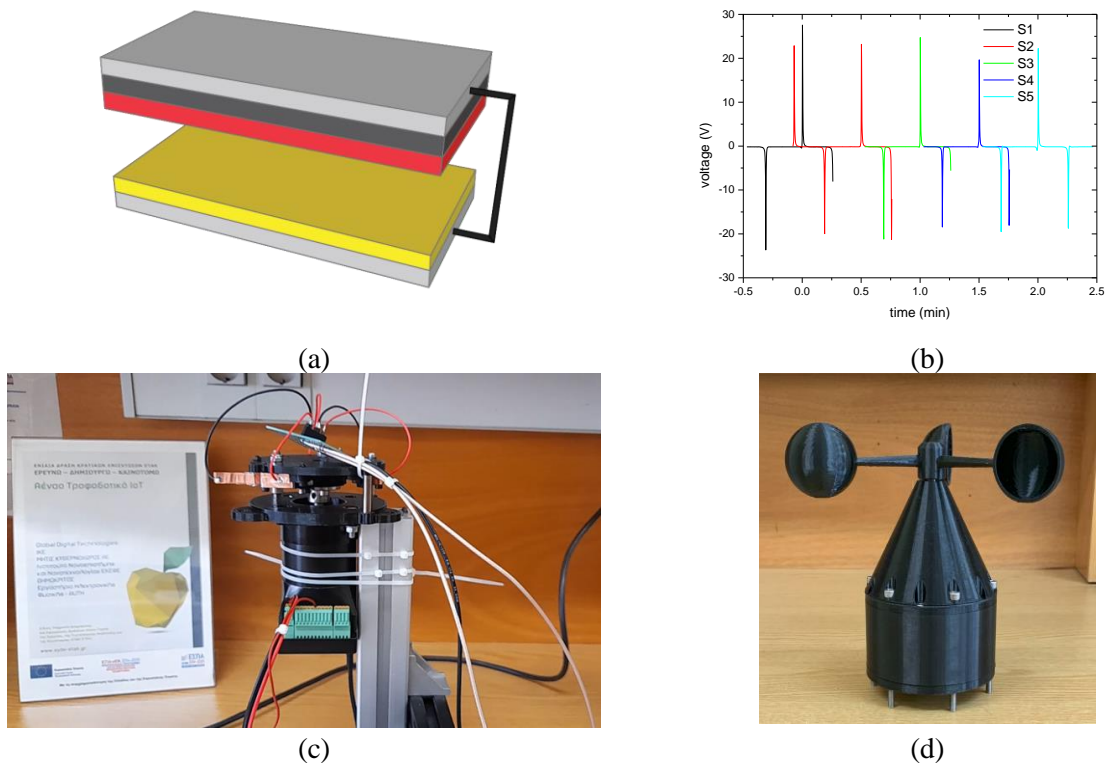

Figure 1. (a) Schematic of a triboelectric device, (b) Typical signals upon contact and separation, (c) Rotating tribogenerator and (d) Harvesting wind energy

[1] F. R. Fan, Z. Q. Tian, Z. L. Wang, Nano Energy 1 (2012) 328-334

Further Evaluation and Calibration of a Mie Scattering-based Apparatus for Portable Optical Haematological Analysis

Asterios Bantis[†1], Maro Michailidou[†2], and Anna Dziuba[3]

Department of Industrial Engineering & Management, International Hellenic University, Greece[1],
Department of Electrical & Computer Engineering, Aristotle University of Thessaloniki, Greece[2],
Faculty of Computing and Telecommunications, Poznań University of Technology, Poland[3]

Abstract—**This paper presents the second stage of data analysis for the "Sappho PDA"; a non-invasive, Mie scattering-based apparatus for portable haematological analysis via optics. In this paper, the dataset presented in [1], is further examined for the generation of statistical indicators and for the validation of previous results.**

Index Terms—**Mie scattering, biomedical sensors, haematological analysis, statistical indicators, embedded systems, optics**

I. Mie Scattering

MIE scattering is the scattering of light as it travels through a medium with a uniform refractive index, like a homogeneous sphere with a diameter larger or equal to the wavelength of light used for the measurement. This scattering of the electromagnetic plane wave is described by the forced oscillations of the electric and magnetic fields according to Maxwell's equations. When analysing biological cells, such as red and white blood cells and platelets, Mie scattering becomes crucial, as these cells' sizes are on par with the light's wavelength. In biomedical applications, Mie's theory is crucial, as it accounts for the complex angle-dependent intensity of the scattered light, with forward scattering typically dominating. The Mie solution, consisting of an infinite series of spherical multipolar partial waves is especially applicable to these cellular components, which are similar in size to λ, and this approach remains valid up to sizes approaching the limits of geometric optics for large particles.[1]

Mie Scattering does not account for the varying morphologies of the cells under observation and considers all measured particles to be spheres; for instance, in our experiments, red blood cells, which are characterised by their biconcave disk shape from a lack of a nucleus, are nonetheless approximated as spheres instead of discoids. Still, even with that approximation considered, Mie Scattering has been the preferred standardised technique for measuring particles smaller than 50 μm since the 1990s, as delineated in the International Standard ISO:13320:2020. This factor establishes its suitability for the current device's operational methodology.[1]

II. The "Sappho PDA" Device

The portable and low-cost device presented is utilising Mie Scattering for detecting particles ranging from 1 μm to 15 μm in diameter. The device is consists of a 650 nm laser, a photodiode array TCD1103GFG produced by Toshiba with a resolution of 1500×1 pixels, the Beaglebone Black rev. C, a custom printed case, and a custom circuit board that facilitates the communication between the photodiode array and the microcomputer. A render of the aforementioned device is shown in figure 1. By measuring the occurring Mie
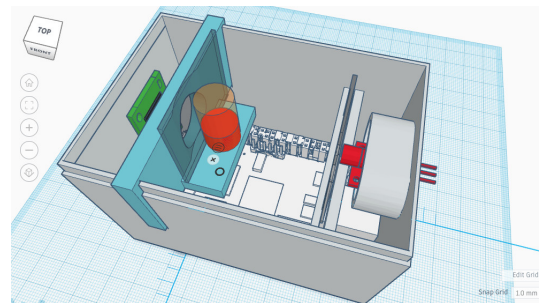
Figure 1: A render of a three-dimensional CAD file of the Sappho-PDA device, with the top cover removed

scattering from the measured cells with the photodiode array, the sensor's output can be examined with statistical analysis in order to approximate the quantity and size distribution of RBCs, WBCs and platelets present.[1][2]

The usage of calibrated solutions of a fixed diameter at 2, 4.8 and 9.6 μm was crucial in confirming the appropriate function of the device and its ability to measure the cells. The size and diameter of WBCs, RBCs and platelets is known from previous research to be about 12-16 μm, 7-8 μm, and 1.5-3 μm respectively, allowing the estimation of the amount of particles present in the solution along with their size.[1] The right half of the measured signal is illustrated in figure 2 for three randomly selected pairs, using particles of a standard diameter and distribution at a specific concentration, comparing unpolarised and polarised samples. The light intensity has been normalised – per sample – to a scale between 0 and 1, using min-max normalisation. Figure 3 illustrates a similar measurement, but for samples taken using aqueous solutions of plant-based beverages, rather than particles of a specific, standardised diameter.

By integrating these documented measurements with the experimental results obtained, it is possible to estimate the concentration and size distribution of the particles within the solution. During past analyses, the authors confirmed, with considerable certainty, that the signals contained in their datasets largely match the expected Mie scattering profiles

predicted by Mie scattering theory, with each experiment exhibiting satisfactory repeatability and accuracy, as previously verified by K. Karakostas.[3][4] Furthermore, the authors have also observed that even using low-cost linear polarisers may reduce optical signal interference and/or improve the measured Mie scattering pattern.[1][2]
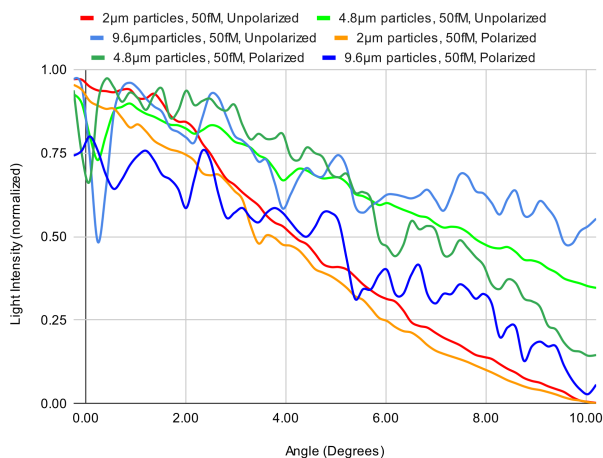

Figure 2: Three random pairs of unpolarised and polarised samples taken for standardised 2μm, 4.8μm, and 9.6μm particles at a 50fM concentration
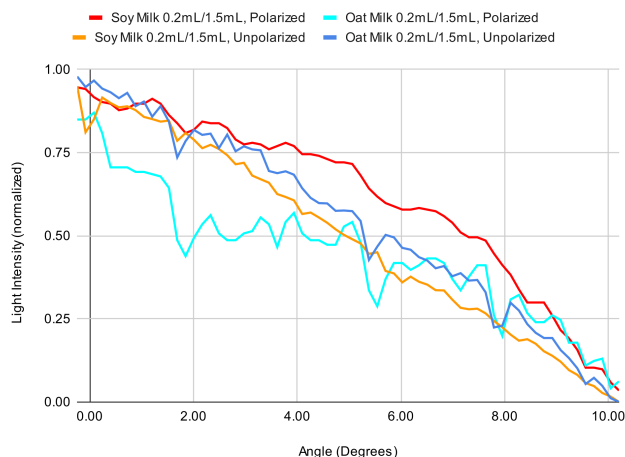

Figure 3: Two random pairs of polarised and unpolarised samples taken for a soy-milk aqueous solution and an oat-milk aqueous solution at a specific % v/v concentration

III. FURTHER ANALYSIS

During the aforementioned stage of analysis, the authors had primarily utilised elements of basic statistics and metrology.[1] Therefore, in this paper, the authors would like to present the second stage of their analysis, in which they've used more advanced algorithms in order to ascertain the accuracy of the previous stage of data analysis. Some of the following algorithms also involve data produced from simulations of Mie scattering theory. MiePlot was used for the generation of these signals.[1]

A. Coherence Test

The coherence test uses both simulated data and experimental data. The result is a single number between 0 and 1, where 0 indicates a total mismatch between the signals, and 1 indicates perfectly-matching signals. In this test, we used nine simulated signals — three for each particle size, for three specific detector distances.[2][5] The results of this test are indicated in table I.

Table I: Lowest and highest coherence ranges for different simulated particle sizes

Sim. Part.	Filter	Low Range	High Range
2μm	Unfiltered	0.05-0.20	0.35-0.60
2μm	2% Mov. Avg.	0.05-0.20	0.40-0.65
4.8μm	Unfiltered	0.10-0.25	0.40-0.60
4.8μm	2% Mov. Avg.	0.10-0.25	0.40-0.60
9.6μm	Unfiltered	0.10-0.25	0.40-0.70
9.6μm	2% Mov. Avg.	0.10-0.20	0.45-0.75

The coherence distribution for 2 μm and for 9.6 μm particles, at different simulated distances from the detector, demonstrates a consistent linear relationship. In contrast, coherence values for particles with a size of 4.8μm do not exhibit a similarly clear linear trend between different distances. The application of a moving average filter, with a size approximately 2% of the length of the original signal, does not mitigate this lack of linearity in the 4.8μm coherence values. Furthermore, the authors observed that due to the simplicity of the theoretical signal, some control signals may test positive as 2 μm signals.

B. K-means Clustering

The authors attempted to use two variations of K-means; the standard "naive" algorithm, and the k-means++ (initialised) method. For k-means++, the algorithm was first initialised with one simulated signal for each particle size, at a specific distance from the detector, for 3 clusters in total. This was later expanded to 9 clusters; one for each simulated scattering pattern mentioned in the header of this section. The results were modest: a marginal improvement over "random guessing" with the naive K-means, and approximately a 7% improvement with k-means++. Further exploration with alternative K-means implementations or other clustering algorithms is required for more significant improvements. Additionally, the utility of K-means could be reconsidered in different use cases, using arrays of results from other tests (i.e. "indicators") as inputs.[2][6]

C. Time-Domain Correlation Tests

The R^2 test was used as "goodness-of-fit" tests in the time domain, in pair with coherence being used as a goodness-of-fit test in the frequency domain. Results can be interpreted similarly to the coherence's results, but the values on the negative axis can be arbitrarily large, depending on the overall lack of determination between the sample and the simulation.[7] The results of this test are indicated in tableII.

In the assessment of R^2 tests at 4.8μm and 9.6μm, a clear linear relationship is observed with the respective coherence tests, indicating a consistent pattern within these wavelength categories. In contrast, the 2μm tests do not exhibit this linear relationship, potentially in part due to control signals testing positive as 2μm signals in the coherence test but not in the R^2 test. The "Pearson's r" test[5] reinforced these findings, providing similar results with variations in numerical values.

Table II: Lowest and highest R^2 distribution ranges for different simulated particle sizes

Particle	Filter	Max. Rng.	Min. Rng.
2μm	Unfiltered	0.75-0.86	(-4.54)-(-3.40)
2μm	2% Mov. Avg.	0.76-0.86	(-4.52)-(-3.41)
4.8μm	Unfiltered	0.67-0.83	(-4.59)-(-3.04)
4.8μm	2% Mov. Avg.	0.67-0.84	(-4.60)-(-3.05)
9.6μm	Unfiltered	0.65-0.82	(-6.92)-(-4.98)
9.6μm	2% Mov. Avg.	0.66-0.83	(-6.92)-(-4.98)

Overall, signals that test positive as a specific particle in coherence tests will often test positive in the R^2 test and the Pearson test.

D. Dynamic Time Warping

The Dynamic Time Warping test was used as an alternative time-domain test, both in order to verify the goodness-of-fit of the two signals, like above, and also as a way to cross-check the outputs of the previous chapter's time-domain tests. In this section, the result represents a measurement of distance between the two signals.[8] Table III presents the results of this test, paired with their corresponding coherence values.

Table III: Coherence and dynamic time warping data for different simulated particle sizes

Part.	Filt.	Min. Rng.	Coherence	Max. Rng.	Coherence
2μm	Unfil.	0.77-2.28	0.35-0.6	5.51-6.52	0.05-0.20
2μm	2% MA	0.75-2.24	0.40-0.60	5.52-6.52	0.05-0.20
4.8μm	Unfil.	1.58-2.64	0.40-0.60	6.33-7.49	0.10-0.30
4.8μm	2% MA	1.54-2.61	0.40-0.60	6.35-7.52	0.10-0.25
9.6μm	Unfil.	1.32-2.56	0.45-0.70	7.30-8.89	0.10-0.25
9.6μm	2% MA	1.26-2.49	0.45-0.75	7.32-8.92	0.10-0.20

Overall, the results exhibited a linear relationship with the results of the coherence test and the R^2 test, especially with the larger particle sizes. Furthermore, similarly to the previous test, control signals with high coherence did not test positive as 2μm waveforms, potentially giving the authors multiple ways to avoid such false-positive outputs.

E. Kolmogorov-Smirnov Test

Ultimately, the authors used the Kolmogorov-Smirnov test's p-value as a "confidence check" for the results of the aforementioned tests. Any p-value larger than or equal to 0.05 in this test indicates that there is a sufficient match between the simulated and experimental signals. In the results, 29.78% of the dataset had individually passed the test with a p-value $\geqslant 0.05$.[5] This is relatively in line with the expected results, under the assumption that not all samples are of equal quality, as approximately 38% of the dataset contains samples of individual calibrated solutions of fixed-diameter particles; 20% of the dataset contains various control samples; 15% of the dataset contains non-standardised aqueous solutions (such as solutions of soy milk, oat milk, salts, etc.); 12% contains in-vivo samples; 10% contains mixed solutions of fixed-diameter particles, and the remaining dataset contains data from minor experiments.

IV. CONCLUSIONS AND FUTURE PLANS

Even though most of the above tests yielded promising results, there is still a requirement for further study. In specific, the authors are planning to experiment with the *wavelet transform* for pattern extraction; with *fuzzy logic* systems, and *supervised* and (other) *unsupervised* machine learning algorithms for data classification from indicators, and with further statistical analysis. In addition, the authors are also planning to implement some of the aforementioned statistical tests into the *K*-means algorithm itself; for example, implementing dynamic time warping rather than Euclidean distance during the training phase. However, a newer, better dataset will be critical for the development and evaluation of several of the above experiments. Last but not least, the authors are exploring enhancements to the physical device, particularly focusing on improvements in computational power, optical properties, and further compliance to European and global standards for biomedical devices, as previously outlined in [1].

REFERENCES

[1] M. Michailidou, A. Bantis, *Scattering measurements with the Beaglebone microcomputer for portable biomedical sensors*, International Hellenic University, 2022

[2] A. Bantis, M. Michailidou, E. Gkagkanis, K. Karakostas and M. E. Kiziroglou, *Fabrication and Development of an Optical Biomedical Sensor*, International Workshop on Microsystems, 2021

[3] Karakostas K., *"Portable system development for Mie scattering analysis, to determine the size of blood cells in in-vivo and in-vitro studies"*, Aristotle University of Thessaloniki, 2019

[4] Konstantinos Karakostas, Stratos Gkagkanis, Korina Katsaliaki, Peter Köllensperger, Alkiviadis Hatzopoulos, and Michail E. Kiziroglou, *"Portable optical blood scattering sensor"*, Microelectronic Engineering 217 (2019) 111129, Elsevier

[5] Pauli Virtanen, Ralf Gommers, Travis E. Oliphant, Matt Haberland, Tyler Reddy, David Cournapeau, Evgeni Burovski, Pearu Peterson, Warren Weckesser, Jonathan Bright, Stéfan J. van der Walt, Matthew Brett, Joshua Wilson, K. Jarrod Millman, Nikolay Mayorov, Andrew R. J. Nelson, Eric Jones, Robert Kern, Eric Larson, CJ Carey, İlhan Polat, Yu Feng, Eric W. Moore, Jake VanderPlas, Denis Laxalde, Josef Perktold, Robert Cimrman, Ian Henriksen, E.A. Quintero, Charles R Harris, Anne M. Archibald, Antônio H. Ribeiro, Fabian Pedregosa, Paul van Mulbregt, and SciPy 1.0 Contributors, *SciPy 1.0: Fundamental Algorithms for Scientific Computing in Python.*, Nature Methods, 17(3), 261-272., 2020

[6] Simon Haykin, *"Neural Networks and Learning Machines"*, McMaster University, Hamilton, Ontario, Canada

[7] Pedregosa et al., *Scikit-learn: Machine Learning in Python*, JMLR 12, pp. 2825-2830, 2011.

[8] Stan Salvador and Philip Chan, *FastDTW: Toward Accurate Dynamic Time Warping in Linear Time and Space*, Florida Institute of Technology, 2007

Remotely Operated Vehicles as a Means of Training Higher education Students in Underwater Surveying

Triantafyllia Anagnostaki, Dimitrios Tziourtzioumis[0000−0002−1881−3953], and
Theodoros Kosmanis[0000−0002−8730−1345]

International Hellenic University, Alexander University Campus, 57400, Sindos, Greece

filliana.anagnostaki@gmail.com

Abstract— **The detailed steps and procedures taken during a hands-on course of a smart marine and maritime surveying postgraduate program are described in this work. The purely practical and experimental course combined with student internship, forced the students to engage themselves to real condition procedures and measurements, focusing in the development of a sensor cluster for the assessment of water quality. Starting from the setup of the sensors and their integration on a Remotely Operated Underwater Vehicle, the course also incorporates the calibration of sensors, their testing in safe and clear water and finally their use in order to assess the environmental conditions of a fish farm. All measurements, performed in two coastal areas of Greece and France, were be uploaded live to the cloud. Although the structure was not combined with Artificial Intelligence during the course, it is designed and developed in order to incorporate bidirectional communication with the Remotely Operated Underwater Vehicle in the near future.**

Keywords— **Marine Surveying Maritime Surveying Training ROUV Environmental Measurements**

I. INTRODUCTION

INTERNET of Things (IoT) and Artificial Intelligence (AI) are technologies that literally rule the technical everyday life for the past decade. There is no technological sector that is not connected even in a small portion with IoT or AI [1]. Towards this direction, a piloting postgraduate course has been implemented during the past three years, offering the participants specialized training on modern subjects and techniques based on IoT and AI for performing surveys and monitoring in maritime and marine applications [2]. The piloting course with the acronym SMARTSEA, produced out of its title "Surveying and MARiTime internet of thingS EducAtion", entails a significant laboratory character. Based on the large scale experiments, the program provides hands-on experience that combines IoT and AI with marine and maritime measurement procedures. This paper presents in details the large scale marine experiments taken place in the frame of SMARTSEA course, as the most challenging activity of the

overall educational scheme that was launched after two years of preparatory work [8, 9]. The experiments are based on a sensoring cluster appropriately developed to measure water quality parameters either as standalone on a testing and calibration phase or adjusted to a Remotely Operated Underwater Vehicle (ROUV), thus providing additional flexibility. It incorporates two typical temperature and pressure sensors and a series of environmental ones, namely Oxygen Reduction Potential (ORP), pH, dissolved oxygen (DO) and conductivity sensors. The calibration procedure as well as the testing and validation phase performed in the coastal areas of Thessaloniki, Greece and la Seyne-sur-Mer, France analyzed in the following sections.

II. MEASURING EQUIPMENT

A cluster of sensors was the basic equipment used by the students in order to perform the on site measurements. The sensor cluster could be implemented either as standalone either attached on a ROUV for more flexibility in underwater measurements. The second part of the equipment was, as mentioned, an ROUV especially acquired for the SMARTSEA educational course [9] (Fig. 1).

Fig. 1. pH and ORP sensors connected to the ROUV.

A. Sensor Clusters

The sensor cluster was composed of six (6) sensors, measuring the Temperature, Pressure, Oxygen Reduction Potential (ORP), pH, dissolved oxygen (DO) and conductivity of the water. Table 1 presents sensors' specifications whereas the communication protocol and port used for their connection with the on board computing platform are presented in [9].

TABLE I
SPECIFICATIONS OF THE SENSOR CLUSTER ITEMS.

Sensor Type	Range	Accuracy
Temperature [°C]	$-45 : +125$	$\pm 2\%$
Pressure [bar]	$0 : 30$	± 0.2
ORP [mV]	± 2000	± 1
pH	$0 : 14$	± 0.001
Conductivity [mS/cm]	$0.01 : 1000$	$\pm 2\%$
Dissolved Oxygen [mg/lt]	$0 : 100$	± 0.05

According to the teaching schedule of the SMARTSEA program, the expected values of the sensors according to the water environment were described and analyzed to the students. Thus, measurements' evaluation was possible. The expected values per sensor are noted below.

Pressure Sensor The pressure sensor is used to indicate the exact depth of the sensor cluster at each measurement. Specifically, one should estimate 1 bar of pressure per 1m of depth.

Temperature In seawater, temperature can be affected by environmental conditions. Factors affecting temperature are sunlight, solar radiation, heat transfer due to convergence of atmospheric flows, and turbidity. Water temperature is a parameter that decreases gradually with increasing depth.

ORP In healthy water bodies, ORP levels should be between 300 and 500 millivolts. ORP is dependent on the amount of dissolved oxygen in the water and the amount of other elements that act like oxygen, such as sulfur (S) and selenium (Se). Low ORP can lead to low dissolved oxygen and increased toxicity of certain metals and contaminants, resulting in many dead putrefactive substances in the water that cannot be purified or decomposed. Such an aquatic environment description does not match a healthy environment for fish and bugs.

pH pH is a measure of the acidity or alkalinity of a liquid solution representing the concentration of hydrogen ions (H+) and hydroxide ions (OH-) on a scale of 0-14. Solutions with a pH below 7 are considered acidic and solutions with a pH above 7 are considered alkaline. The average pH of the ocean is about 8.1, meaning basic or alkaline. However, human activity has fundamentally changed the chemical composition of the ocean leading to a drop in seawater pH, a phenomenon called ocean acidification that threatens marine ecosystems.

Dissolved Oxygen Dissolved oxygen (DO) refers to the amount of unbound free oxygen present in the water. It constitutes a parameter that evaluates water quality based on the impact on organisms inhabiting the water area. Dissolved oxygen levels can be high or low. Both can harm aquatic life and affect water quality. The dissolved oxygen concentration in seawater is typically 7 to 8 milligrams per liter (mg/lt). Dissolved Oxygen is affected by phenomena like diffusion, aeration, photosynthesis, respiration, and decomposition, while it varies significantly with temperature, pressure, and salinity. The solubility of dissolved oxygen decreases with increasing temperature, meaning that larger depths dis- solved oxygen is expected to be lower.

Conductivity The conductivity of a solution, that is concentration of ions in water is a measure of its ability to conduct electricity, sound, and heat. The conductivity of seawater depends on temperature and salinity and is independent of pressure (depth). Salts such as sodium chloride (NaCl) dissociate in water to form cations and anions that migrate in the presence of an electric field to generate an electric current. As a result, conductivity increases with the concentration of dissolved salt, i.e. salinity. In addition, the conductivity increases with increasing temperature due to the increased ion mobility. Sea water has a typical conductivity between 30 mS/cm and 60 mS/cm.

B. Remotely Operated Underwater Vehicle

The sensor cluster was hosted by an appropriately developed ROUV. The vehicle used for the measurements was based on the Blue ROV2 model of Blue Robotics [10], the chassis of which was modified in order to host the extra environmental sensors. Similarly, a graphical user interface (GUI) was developed in order to acquire sensor data and upload them on the cloud [9]. Besides the sensors, it is worth mentioning that the ROUV operation is powered by a 14.8V, 15.6Ah Li-ion battery providing an average of 2h autonomy under constant thruster use.

III. MEASUREMENTS

The equipment described in the previous section was utilized by the students in two cases. As it was important for the sensors to be tested in a real water environment, the two sets of measurements took place in coastal areas, one clear of any aquatic entrepreneurial activity in Thessaloniki, Northern Greece and one in the premises of a fish farm in La Seyne-sur-Mer, Southern France (Fig. 2). Initially, and prior to any measurements at sea, the sensors were calibrated. Afterwards, a test measurement procedure was followed in order to stress the equipment under the real conditions. The water proof of the ROUV chambers was checked as well as the ability of the sensors to provide rational, in the expected range measurements. It is noted that all procedures were performed by the students as part of their training, under appropriate supervision. The educational added value lies not only in the preparation phase of the equipment or in the measurements themselves but also in the post-measurement procedure, when the outcomes had to be assessed. Data were acquired via the secure shell (ssh) protocol and uploaded to the cloud enabling any possible bidirectional reaction, e.g. ROUV depth stabilization or specific movement.

A. Sensor's Calibration

Essential to improve sensor performance, calibration procedure was preceded any measurement performed. The procedure took place in two parts. First, the temperature and pressure sensors, built in the ROUV, were calibrated through the ROUV control software. The four environmental sensors were calibrated via a specific procedure defined by the manufacturer using appropriate chemical solutions. The sensors were put in sample liquids and their control software was adjusted to read each sample as an appropriate value. At the end, all sensors were able to measure according to their respective range.

Although trivial for any measuring equipment, the calibration procedure had to be performed by the students themselves in order to realize its significance.
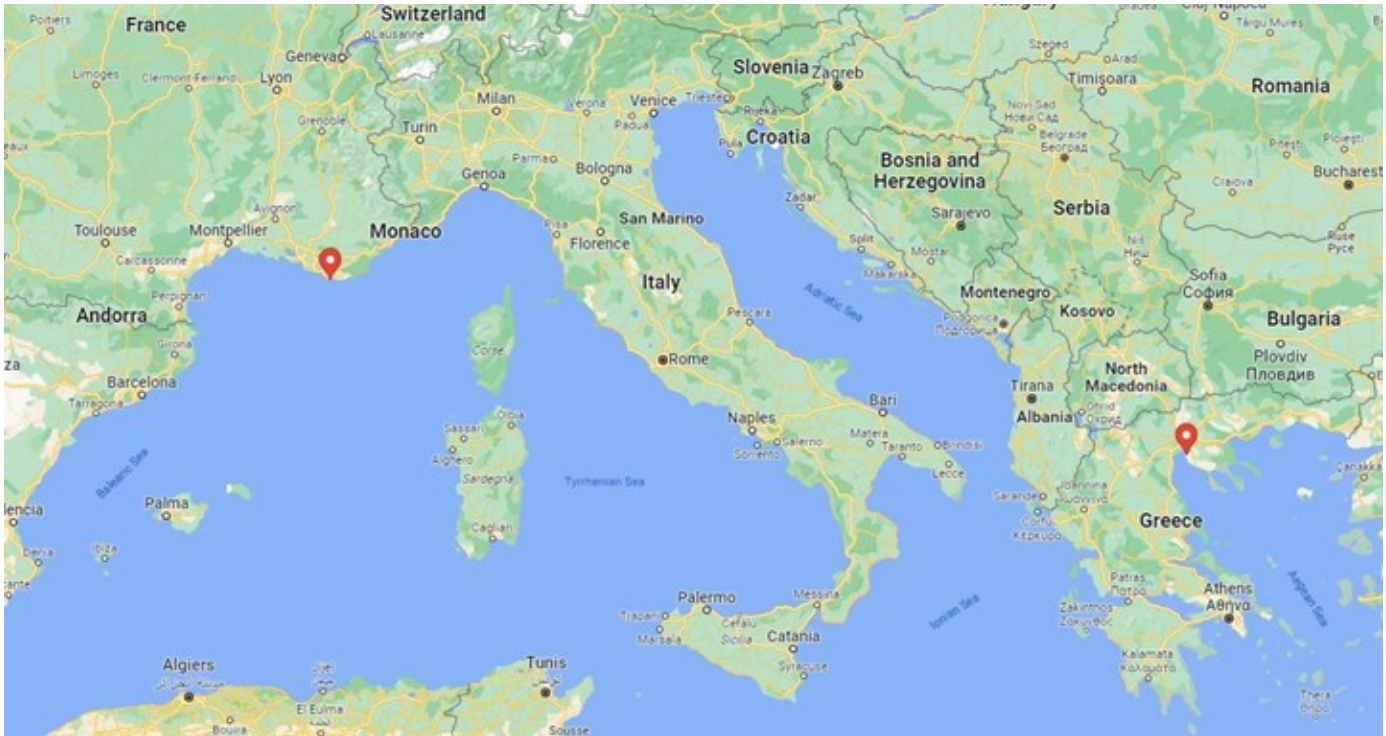
Fig. 2. Map with the locations of test measurements in Greece and France.

B. Measurements in Greece

The first set of measurements took place in the coastal area of Thessaloniki prefecture in Northern Greece on June 1st 2022. The area characterized by the absence of any aquatic entrepreneurial activity that would cause the water parameters to deviate from their typical values, was ideal to test the ability of

Fig. 3. Measurements points in a coastal area in Thessaloniki, Northern Greece.

the environmental sensors to measure correctly. Additionally, the ROUV chambers accommodating the battery and the electronic components was tested for being leak-proof. Thus, a series of tests from an appropriate checklist has been performed prior to any ROUV dive. Measurements from the sensors were taken along various paths and depths up to 2m, as the waters were shallow. Such a path is depicted in Fig. 3 whereas in Table 2 the values acquired by all sensors in the three measurement spots 3, 4 and 5 at a constant depth of 1.5m are presented. The spots are characterized as points G3, G4 and G5, with direct correspondence to points 3, 4 and 5 of Fig. 3. The results were

typical of environmentally healthy sea water, according to the description of section 2, with sensor values being relatively constant.
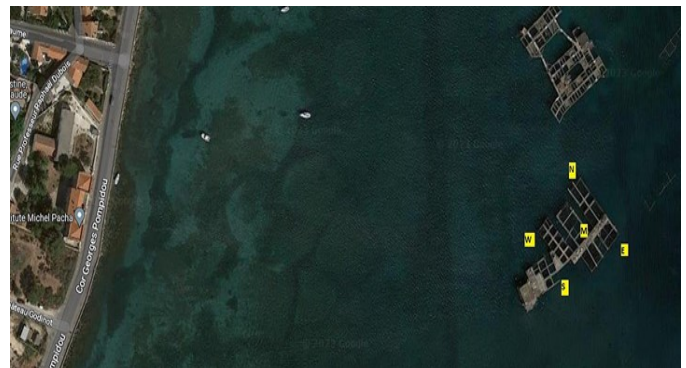

Fig. 4. Measurements points around a fish farm in La Seyne-sur-Mer, Southern France.

TABLE II
SPECIFICATIONS OF THE SENSOR CLUSTER ITEMS

Sensor Type	G3	G4	G5	FW	FN	FS	FE
Conductivity [mS/cm]	48.1	48.2	48.4	56.99	56.92	56.97	56.97
ORP [mV]	115.1	115.0	115.1	–	–	–	–
pH	8.75	8.77	8.73	8.20	8.20	8.17	8.19
Dissolved Oxygen [mg/lt]	6.36	7.31	7.76	7.89	7.92	7.90	7.91
Temperature [^oC]	25.8	25.2	24.8	24.9	24.7	24.7	24.8

C. Measurements in France

The second set of measurements took place around a fish farm in La Seyne-sur-Mer, Les Sablettes, France on June 29th 2022 in the frame of the industrial internship of the students.
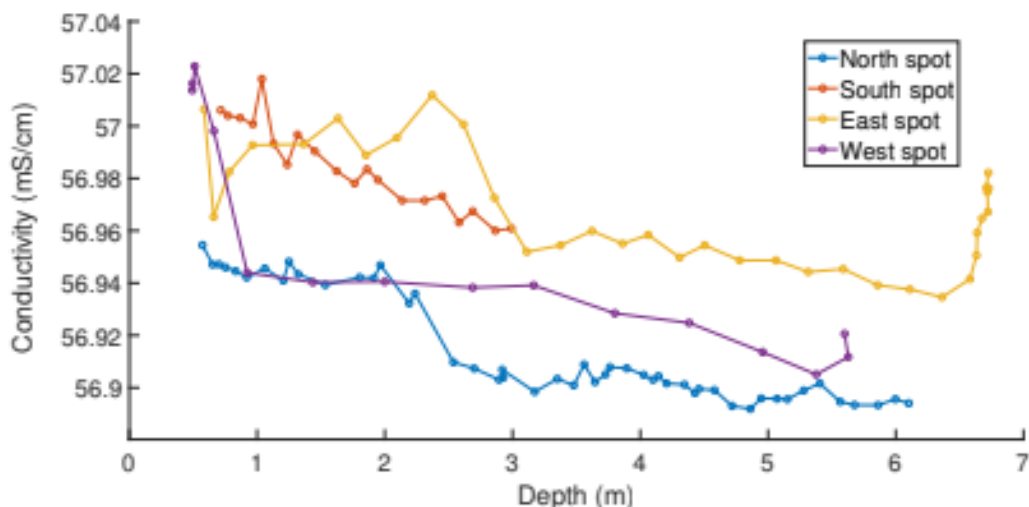
Fig. 5.Conductivity graph versus depth from the four measuring spots around a fish farm in La Seyne-sur-Mer, France.

The sensor cluster was already calibrated and tested and could be used for the assessment of the water quality around the fish farm (Fig. 4). Indicatively, data were acquired at four (4) measurement spots around a fish cage and one in the middle of it. Table 2 presents the average values of the data acquired from each sensor at the specific spots around the fish cage (FE, FN, FW, FS correspond to E, N, W, S respectively). Averaging was performed on all values acquired by each sensor from each spot during a dive from the sea surface until a maximum depth of about 7m. The variation of values measured per sensor along this distance was insignificant as depicted in Fig. 5. Similar results with those taken from the first measurement set in Thessaloniki district were observed, as expected since the water quality was equally good. Apparently, any deviation would be an indication of abnormal water conditions. The findings were similar as those of the first set in Greece. It is noted that due to a sudden, irreversible sensor fault, no ORP data were possible to be acquired.

D. Conclusions

As the need to increase the use of smart measuring equipment and approach in maritime and marine sector increases, the procedures of a purely laboratorial course in the frame of SMARTSEA postgraduate program was presented in this paper. The development and calibration of a sensor cluster was initially described. The measurements performed in two coastal areas of different characteristics were presented emphasizing mostly on the safety procedures and the acquisition of reliable sensor values. The overall structure provides increased flexibility as connected in a wireless network it can provide remote access to underwater premises by means of the IoT technology, fully aligned with the current trends of marine and maritime sector.

IV. COPYRIGHT

All content included in this submission, including but not

limited to text, figures, tables, and supplementary materials, has been created by the authors listed in the submission email.

REFERENCES

[1] OECD: Artificial Intelligence in Society. OECD Publishing, Paris (2019).

[2] Cancela, J.-J., Gonzalez , X.-P., Vilanova, M., Mirás-Avalos, J.-M.: Water Management Using Drones and Satellites in Agriculture. Water. **11**(5), 874 (2019). https://doi.org/10.3390/w11050874

[3] Chen, C.-H., Wu, Y.-C., Zhang, J.-X., Chen, Y.-H.: IoT-Based Fish Farm Water Quality Monitoring System. Sensors. **22**(17), 6700 (2022).

[4] Lafont, M., Dupont, S., Cousin, P., Vallauri, A., Dupont, C.: Back to the future: IoT to Improve Aquaculture : Real-Time Monitoring and Algorithmic Prediction of Water Parameters for Aquaculture Needs. 2019 Global IoT Summit (GIoTS), Aarhus, Denmark, pp. 1-6 (2019). https://doi.org/10.1109/GIOTS.2019.8766436

[5] Adhipramana, M., Mardiati, R., Mulyana, E.: Remotely Operated Vehicle (ROV) Robot For Monitoring Quality of Water Based on IoT. 2020 6th International Conference on Wireless and Telematics (ICWT), Yogyakarta, Indonesia, pp. 1-7 (2020). https://doi.org/10.1109/ICWT50448.2020.9243614

[6] Kabanov, A., Kramar, V.: Marine Internet of Things Platforms for Interoperability of Marine Robotic Agents: An Overview of Concepts and Architectures. Journal of Marine Science and Engineering **10**(9) pp. 1279 (2022).

[7] SMARTSEA MSc homepage, http://www.smart-sea.eu, last accessed 2023/03/12.

[8] Kravari, K., Tziourtzioumis, D., Kosmanis, T.: AIRUV: A remotely operated underwater vehicle with artificial intelligence perspectives. In: S. Rodríguez González et al. (Eds.): Distributed Computing and Artificial Intelligence. 1242 AISC, 116–125 (2021). https://doi.org/10.1007/978-3-030-53829-3_11

[9] Charitonidis, A., Tziourtzioumis, D., Kravari, K., Kosmanis, T.: Marine Surveying Education by Implementing Artificial Intelligence on Remotely Operated Underwater Vehicle Sensors. In: S. Rodríguez González et al. (Eds.): Distributed Computing and Artificial Intelligence, Volume 2. 332 LNNS (2022). https://doi.org/10.1007/978-3-030-86887-1_10

[10] Blue Robotics inc. homepage, http://www.bluerobotics.com, last accessed 2021/05/25.

Utilization of fermentable biomass for bioethanol production and design
of sustainable modular energy storage liquid fuel unit

[1] Koumpakis Dimitrios-Aristotelis koumpakisd@gmail.com

Tziourtzioumis Dimitrios dtziour@gmail.com

Abstract **- This paper investigates the viability of utilizing bioethanol as a sustainable alternative to gasoline, focusing on the development of an automated modular unit. The study explores the utilization of waste peaches from local peach industries as a feedstock for bioethanol production. In this innovative approach, surplus energy from the electricity network and biomass oriented by the agricultural peach industry are harnessed. The modular unit is designed to efficiently convert waste from table peaches into bioethanol and other valuable by-products. The research delves into the technical and economic feasibility of this bioethanol production system, addressing key challenges such as scalability, environmental impact, and resource optimization. The findings contribute to the growing body of knowledge on renewable energy sources, offering a sustainable solution for biofuel production that aligns with the principles of circular economy and agricultural waste utilization.**

Index Terms **- bioethanol, energy storage, modular design, waste to energy, biofuels, industrial automation**

I. INTRODUCTION

Bioethanol, a promising biofuel, offers a transformative solution to contemporary energy challenges. Utilizing existing technologies and infrastructure akin to conventional petrol products, bioethanol represents a sustainable alternative. Amidst the looming energy crisis, bioethanol stands out for its capacity to contribute to a decentralized energy production model, reducing reliance on global markets. Notably, its environmentally friendly attributes make it a crucial player in mitigating climate change, with reduced greenhouse gas emissions. Bioethanol provides flexibility in energy distribution as it can contribute to the storage of other forms of energy [2]. This study explores an innovative approach, utilizing waste peaches from local industries, aligning with circular economy principles and presenting a realistic perspective to zero waste and energy management concerns.

II. HISTORICAL BACKGROUND

Bioethanol's history traces back to its initial use in engines in 1908, but the 20th and 21st centuries predominantly favored gasoline. The oil crises of 1973 and 1979, pivotal moments in global energy dynamics, prompted a shift. Internationally, cars were redesigned for multi-fuel compatibility, ushering in an era where gasoline blended with ethanol gained prominence. This strategic adaptation not only addressed energy security concerns but also paved the way for the renewed significance of bioethanol as a viable and sustainable component in the automotive fuel landscape, positioning it as a key player in the quest for greener and more resilient energy solutions. [5][6]

III. BASIC PRINCIPLES

This fuel, which name is a derivative of ethanol or alcohol, undergoes a transformative process starting with fermentation of agricultural products. Later, it is being distilled just like the consumable alcohol, but bioethanol takes a critical turn when reaching the azeotropic point. At this juncture, the distillation requires dehydration to achieve 100% anhydrous ethanol, devoid of water content. This waterless ethanol is then blended (or not) with different rates of gasoline for commercial use in internal combustion engines [7][4]. Experimentation has also been conducted in enydrous bioethanol however, without yielding results suitable for large scale production.
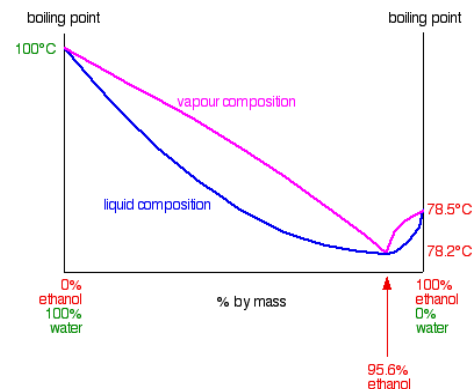

Fig. 1. Azeotrope mixture of ethanol and water [9]

TABLE I
PROPERTIES OF BIOETHANOL

|	**Physical and chemical properties**	
1	Density	789,3 kg/m3
2	Condition at atmospheric pressure	Liquid
3	Color - Smell	Colorless with characteristic odor
4	Melting temperature	-114,5 °C
5	Boiling temperature	78,37 °C
6	Ignition temperature	13–14 °C
7	Self-ignition temperature	362 °C
8	Viscosity	1,2 mPa·s at 20°C
9	Solubility in water	Mixed in every proportion
10	Octane rating	100 - 135
11	Cetane rating	2 – 12
12	Energy content (calorific value)	LHV - 27 MJ/kg , HHV - 29,7 MJ/kg
13	Symbol of ADR (refers to a category of risks during its storage and transport)	Flammable (**F**)
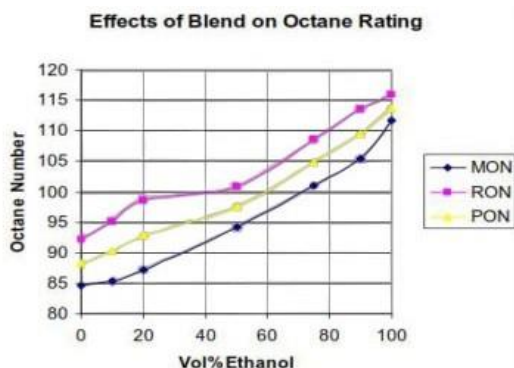
Fig. 2. Octane rating in different ethanol-gasoline blends. [8]
MON (Motor octane number), RON (Reaserach Octane Number)
PON (Average of RON and MON)

IV. CASE STUDY

As of 2021, according to ELSTAT data, the regions of Imathia and Pella, proximate to Thessaloniki, boasted the world's largest peach production in a relatively compact area, yielding an impressive 5.9 and 8.8 million tons respectively. Despite this abundance, a notable 10-28% of peaches are being discarded or a part of those are used further for juice production. Addressing this inefficiency, this innovative unit capitalizes on this substantial waste, diverting it towards the commercial production of bioethanol.

Peaches, containing approximately 9% sugars, constitute a valuable resource for ethanol production. Additionally, the varying pectin content (0.1-0.9%) in discarded peaches contributes to methanol production. It was estimated that from only the 3% of the 8.8 million tons of peaches, approximately 15.36 million liters of ethanol could be produced, taking into account the sugar content and the density of ethanol, which is about 0.789 kg/L. Additionally, based on the pectin content and considering the density of methanol at approximately 0.791 kg/L, the methanol yield from this massive quantity of peaches could reach 901.138 liters.

This side industrial unit, operating on a mini scale, automates the production of bioethanol and its byproducts, including methanol for fuel, CO2 for beverage industries, animal feed, syngas bottles, and biodiesel. This substantial production volume not only has the potential to meet the entire annual agricultural fuel needs of the area but also offers the opportunity for exporting surplus biofuels [3]. Moreover, the by-products generated during the biofuel production process could further contribute to economic and environmental benefits, emphasizing the sustainable and circular approach of utilizing peach waste in the region's agricultural and energy sectors.

Operating in tandem with a peach processing facility, the unit harnesses energy from peach biomass, such as stalks and pruning. Moreover, it seamlessly integrates with the power grid, utilizing surplus electricity during periods of abundance. This not only fully harnesses the produced energy, but also establishes a method of storing excess electricity in the form of bioethanol and other valuable byproducts, thus contributing to a zero-waste prototype and fostering the development of alternative environment friendly fuels.

The technological framework of this unit extends beyond energy utilization. It incorporates smart electricity meter and artificial intelligence to predict and manage surplus energy, optimizing the side plant's efficiency. This holistic approach not only transforms discarded peach waste into valuable resources but also exemplifies a sustainable model for biofuel production, addressing both environmental concerns and energy sustainability.

The preparation, production, and storage processes of this bioethanol unit are expertly automated using Structured Text (ST) language, incorporating commands, loops, electrovalves, pumps, and circulators for efficient operation. The detailed workings of the system are meticulously outlined in the provided Piping and Instrumentation Diagram (P&ID), offering a comprehensive visual guide of the unit's complex functionality and interconnections.

More specifically
In the preparation process:

➢ Stored fruits, whether in warehouses or outdoor spaces, are moved to a day silo.
➢ Upon a human operator's start command, the material is transferred via a belt to a pulper-shredder for easier handling and sugar release.
➢ The pulp is then led to a fermenter where the temperature gradually increases to 80 degrees Celsius to pasteurize the mixture, preventing microbial contamination.
➢ Fresh water is added for mixture homogenization, with automatic material quantity adjustments based on "high-high" and "high" automation logic.
➢ The mixture cools to 30 degrees Celsius before yeast, dissolved in water and warmed to the same temperature, is added.[1]
➢ A biomass boiler, utilizing dry biomass from pruning, stems, and peach pits, provides heat. In case of fuel shortage, biomass pellets are used.
➢ Heat transfer occurs through a hydraulic system using stainless steel pipes to prevent oxidation, maintaining accuracy and modularity for system expansion.
➢ The mixture ferments for 10 days in the fermenter, with daily stirring from a base-mounted mixer.
➢ Ten fermenters are used to repeat the process daily.
➢ CO2 released during fermentation is stored in an air tank through non-return valves υor sale to beverage industries.
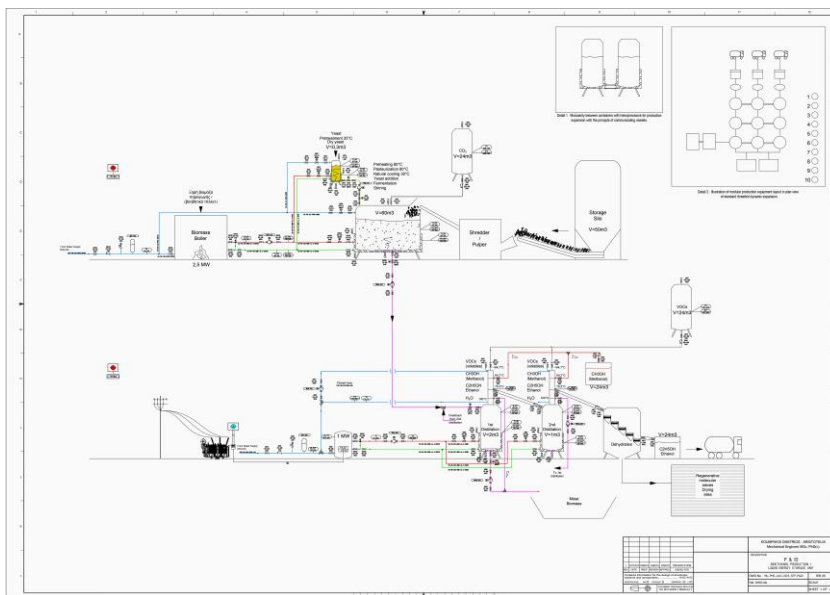
Fig. 3. P&ID of process unit

In the production process:

> ➢ The fermented mixture is divided into various systems for efficient bioethanol extraction, utilizing by-products.
> ➢ The first distiller, heated by a rapid heater with electric resistance, is activated automatically when excess electricity is detected in the network.
> ➢ A separate low-voltage three-phase line, monitored by a smart meter, powers the resistance, optimizing both provider and consumer processes.
> ➢ An AI system uses these data for predictions and statistical analyses to improve operational processes.
> ➢ The distillers, smaller than fermenters and batch-fed, quickly heat the mixture for efficient distillation.
> ➢ The heating water in the jackets is superheated to over 100 degrees Celsius at 2 bar pressure for continuous distillation.
> ➢ A fractional distillation column at the top separates water, ethanol, methanol, and other volatiles.
> ➢ Ethanol (about 50% concentration) proceeds to a second distillation to reach its azeotropic point (95.6%).
> ➢ Methanol is stored in liquid tanks, while volatiles are in gas tanks. When tanks are full, they are transported by truck.
> ➢ Remaining solids from the first distillation are used for biodiesel production or animal feed.
> ➢ Water from the second distillation, still containing ethanol, is recycled back to the first distillation.
> ➢ Ethanol at 95.6% passes through a molecular sieve tank for moisture removal, with sieves periodically replaced for reactivation.
> ➢ The process continues uninterrupted with a backup batch of sieves.

In addition to the design, calculations, and automation, the project involved practical experimentation in mini-scale ethanol production using household equipment. These hands-on experiments were conducted in alignment with the principles outlined in the designed unit, providing valuable insights into the feasibility and scalability of the innovative bioethanol production process.

Fig. 4 Distillation and final bioethanol combustion

REFERENCES

[1] Azhara, S. H. M. et al., 2017. Yeasts in sustainable bioethanol production: A review. *Biochemistry and Biophysics Reports, Vol* 10, pp. 52-61.

[2] Danúbia Paula Cadore Favaretto. et al, 2023. Fruit residues as biomass for bioethanol production using enzymatic hydrolysis as pretreatment. *World Journal of Microbiology and Biotechnology,* Vol 39, p. 144.

[3] Goldman et al, 2011. *Scientific challenges of bioethanol production in Brazil,* Piracicaba, SP, Brazil: Appl Microbiol Biotechnol.

[4] Nibedita Sarkar et al, 2012. Bioethanol production from agricultural wastes: An overview. *Renewable energy ,* Vol 37, pp. 19-27.

[5] Srivastava, N. & Mishra, P. K., 2022. *Food Waste to Green Fuel: Trend & Development.* Varanasi: Clean Energy Production Technologies.

[6] Vohra, M. et al, 2014. Bioethanol production: Feedstock and current technologies. *Journal of environmental chemical engineering,* Vol 2, pp. 573-584.

[7] Wyman, C., 1996. Handbook on Bioethanol: Production and Utilization. USA: Taylor&Francis.

[8] Brown, C., 2018. Introduction of E10 Gasoline to Ireland,Supply Chain Implications. EERL.

[9] Raosaheb, P. S., 2015. Steady state simulation of an Azeotropic Distillation system using Aspen Plus, Rourkela: National Institute of Technology Rourkela.